Simulations of the Galactic Center for *Athena*

Bachelorarbeit aus der Physik

Vorgelegt von

Matthias Rohe

23. August 2022

Dr. Karl Remeis-Sternwarte Bamberg
Friedrich-Alexander-Universität Erlangen-Nürnberg

Betreuer: Prof. Dr. Jörn Wilms

Abstract

In this thesis I present and analyze several observations of the Galactic Center for the WFI and X-IFU with *Athena* using the simulation software SIXTE. These simulations are based on a *Chandra* catalog from Muno et al. (2009) which includes 9017 sources of the central $2^\circ \times 0.8^\circ$ field. I explain the process for the final input file for the simulations of the Galactic Center and present images for the WFI and X-IFU. These images demonstrate the capabilities of *Athena* (especially the WFI) with an exposure time of just 100 ks. I show an RGB image with the WFI and find out from this that the sources vary in the energy band in which they are detectable and that their color match their assigned spectral model which was calculated with their Hardness Ratios. I compare the color scheme of this RGB image with a map of the hydrogen color density of the Galactic Center and figure out that the correlation between them is clearly visible. Also, I find out that about 44 % of all sources in the field of view of the WFI are detectable in the final image. This detection probability proves to be depending on the angular separation of the sources. In the final section, I compare the simulation images with archival images from *Chandra*. The simulation images are capable of a similar product with just a fifteenths of the exposure time due to *Athena*'s larger effective area.

Contents

List of Acronyms

Athena	Advanced Telescope for High-ENergy Astrophysics
CDS	Centre de Données astronomiques de Strasbourg
CIAO	*Chandra* Interactive Analysis of Observations
CMZ	Central Molecular Zone
CND	CircumNuclear Disk
CTTS	Classical T Tauri Star
DEPFET	DEPleted Field Effect Transistor
ESA	European Space Agency
FITS	Flexible Image Transport System
GC	Galactic Center
HEASARC	High Energy Astrophysics Science Archive Research Center
HMXB	High-Mass X-ray Binary
HR	Hardness Ratio
LMXB	Low-Mass X-ray Binary
MS	Mini-Spiral
NASA	National Aeronautics and Space Administration
NSC	Nuclear Stellar Cluster
NuSTAR	Nuclear Spectroscopic Telescope ARray
Sgr A*	Sagittarius A*
SIMPUT	SIMulation inPUT
SIXTE	SImulation of X-ray TElescope
SPO	Silicon Pore Optics
TTS	T Tauri Star
WFI	Wide Field Imager
WR	Wolf-Rayet
WTTS	Weak-lined T Tauri Star
X-IFU	X-ray Integral Field Unit
XML	eXtensible Markup Language

1 Introduction

The first extraterrestrial radio source was found in 1933 by Karl Guthe Jansky. The detected signal came from the constellation Sagittarius and was named Sagittarius A. After that, it took over 40 years to discover Sagittarius A* (Sgr A*) as a discrete object (Bryant and Krabbe; 2021). After these breakthroughs, high-resolution imaging throughout the electromagnetic spectrum became more powerful with the time. Until today, the Galactic Center (GC) is a very popular target for observations because of its supermassive black hole and the unique characteristics in its surroundings (Witzel et al.; 2017). Most recently, the first observations with the Event Horizon Telescope of Sgr A* were published. This is shown in Figure 1.1. The image validates the assumption of a supermassive black hole in the center of our galaxy as it shows the Event Horizon of Sgr A* (Hensley; 2022).

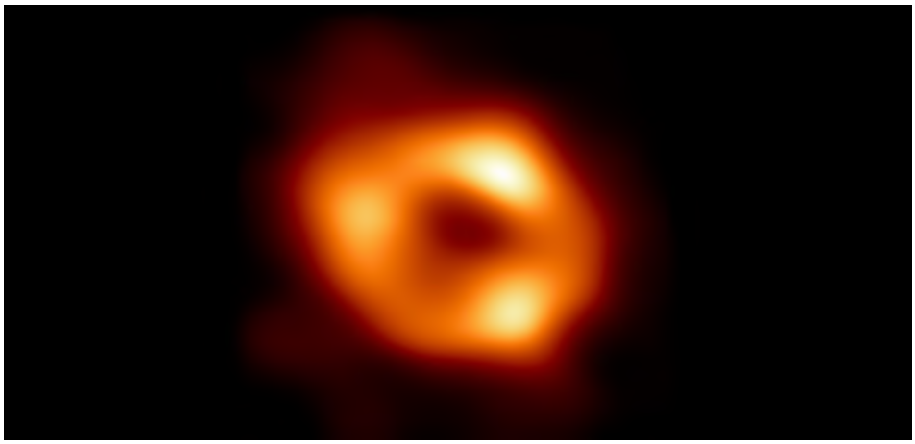

Figure 1.1: Image of the Event Horizon of Sgr A* recorded with the Event Horizon Telescope. Image from Hensley (2022).

Due to its proximity to us of just 8 kpc, the stellar population around Sgr A* is a great laboratory to study nuclear star clusters (Feldmeier-Krause et al.; 2017). In the larger environment of the GC (radius of a few hundred parsecs) lies an astonishing number of young and massive stars with an immense star formation rate (about 10 % of all stars form in the GC). Every fourth Wolf-Rayet (WR) star is located in this region. Because of the resulting density of star formation and massive stars, the GC provides a great environment to understand the evolution of stars (Stolte; 2013).
In their life cycle, stars are detectable as X-ray sources. Massive early-type stars emit X-rays because of shocks in their stellar winds, while the high magnetic activity of pre-main-sequence stars cause them to produce X-rays. As a consequence of this, X-ray astronomy marks an important area to understand the properties of stellar objects (Muno et al.; 2009). In order to measure these incoming X-rays, many different missions were funded. The two main active X-ray telescopes are *Chandra* from NASA and XMM-Newton from ESA. Renderings of the spacecrafts of the two missions are shown in Figure 1.2.

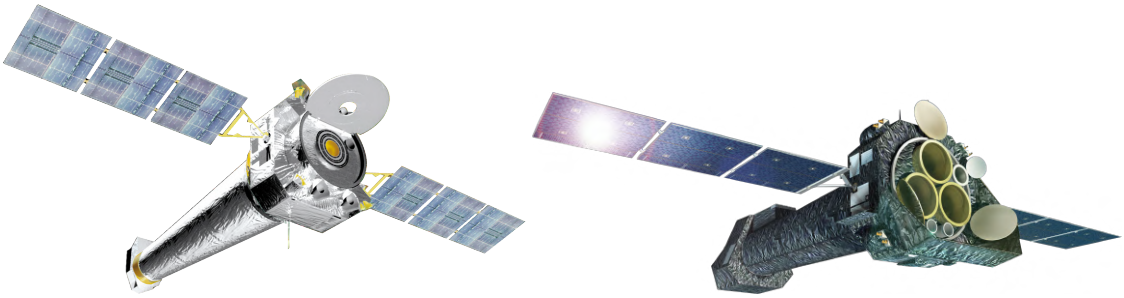

Figure 1.2: Renderings of *Chandra* (left) and XMM-Newton (right). Images from NASA[1].

Athena will be the future X-ray mission from ESA with a much larger effective area and higher energy resolution than any other X-ray telescope. Because of these properties, *Athena* will likely make breakthroughs in many different fields of astronomy (Barret et al.; 2020). In order to show the capabilities of this mission, I will present simulations of the GC with *Athena* and show images that indicate the imaging performance of the WFI.
The remainder of this thesis is structured as follows. In section 2 I will introduce Athena in greater detail. In section 3 I will explain the structures of the GC, followed by the origins of X-ray emission from stars and X-ray binaries in section 4. After that, I will give an overview of the simulation software SIXTE (section 5) and introduce the used source catalog (section 6). Then, in section 7, I will present several simulations of the GC and analyze them. Lastly, I will draw conclusions from these simulations (section 8).

[1] `https://science.nasa.gov/get-involved/toolkits/spacecraft-icons`

2 *Athena*

Athena (Advanced Telescope for High-ENergy Astrophysics) will be an X-Ray telescope developed by ESA, which is set to launch in the early 2030s into space. The science theme of this mission "The Hot and Energetic Universe" addresses two main questions. The first one is how the large-scale structures in the universe are assembled by baryonic matter. The second one is the impact of black holes on the shape of the universe and to understand their growth as well. In order to answer these questions *Athena* is provided with three main technical components: An X-ray telescope, an X-ray Integral Field Unit (X-IFU) and a Wide Field Imager (WFI) (Barret et al.; 2020).
The planned design of the spacecraft is shown in Figure 2.1. The WFI and X-IFU are at the back in the Focal Plane Module. The mirrors of the telescope are located in the front and are mounted to the Service Module. These two components are connected via the Fixed Metering Structure which also holds the large solar panels (spread of over 26 m) for the power supply (Brand; 2017).

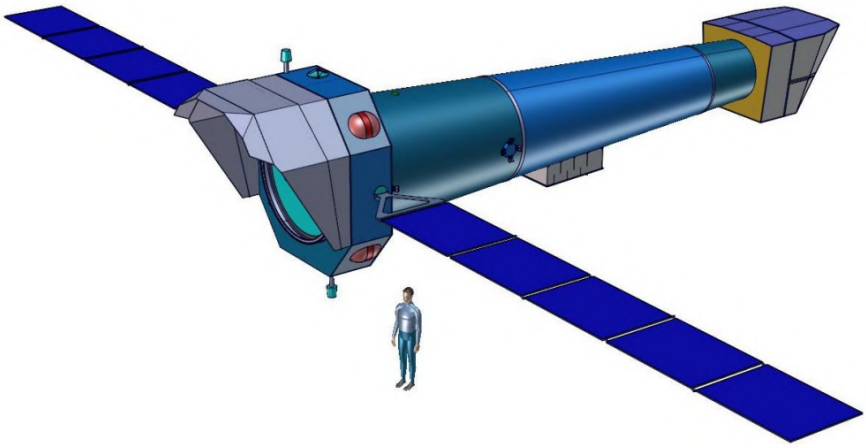

Figure 2.1: Design rendering of *Athena*. At the back are the technical instruments (WFI and X-IFU) which are connected to the Service Module in the front by the Fixed Metering Structure between them. For a size comparison, an average human is depicted beside the spacecraft (Ayre et al.; 2016).

2.1 The Optics

The telescope will have a focal length of 12 m and the effective area at 1 keV amounts to around 1.4 m^2. While aiming for this effective area, *Athena* will also maintain an angular resolution of 5″ Half Energy Width. All that is possible because of the innovative Silicon Pore Optics (SPO) that the mission will use for its mirror (Barret et al.; 2020).

The mirror follows the Design of a Wolter telescope. A Wolter telescope solves the problem of the small refractive index of X-rays. It uses a paraboloid shape of the mirror, followed by an hyperboloid. Because of the rather small effective area of just one mirror like this, many mirrors with different radii but the same focal length of 12 m are built inside each other. An example of a stack of the silicon plates used for *Athena* is shown in Figure 2.2. Each pore of this SPO acts like a Wolter-type mirror to focus the incoming X-rays at the back in the Focal Plane Module. In order to select between the WFI or the X-IFU, the mirror of *Athena* is movable. The mirror can be tilted in such a way that the incoming X-rays are only illuminating the chosen detector (Brand; 2017).

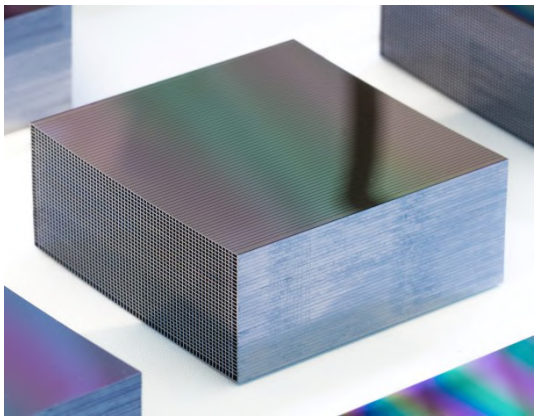

Figure 2.2: A SPO mirror stack with 35 layers of silicon plates. Each pore acts as a Wolter mirror to refract the X-rays back to the Focal Plane Module. Image from Collon et al. (2016).

With these optical elements *Athena* will have a significantly better energy resolution and total effective area than any X-ray spectrometers which are planned or exist. Because of that the mission will be able to make significant discoveries in almost the entire astrophysics in its expected four years lifetime (Barret et al.; 2020).

2.2 The WFI

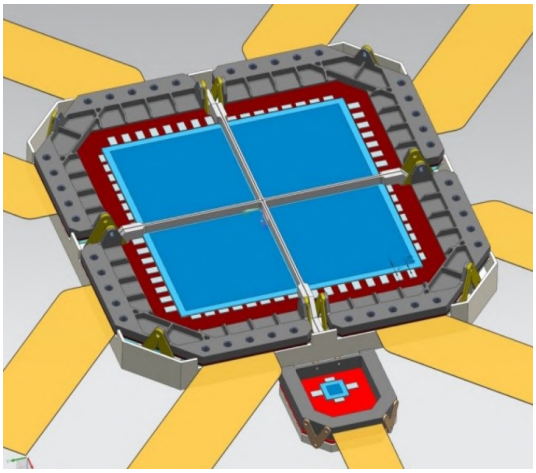

Figure 2.3: Image of the design of the WFI with the the four main DEPFETs (blue) and the small one for bright sources at the bottom. Image from Meidinger et al. (2015).

The WFI is a very powerful spectral-imaging camera with an energy resolution of roughly 170 eV at 7 keV. It is based on a unique Silicon technology and will provide a field of view of $40' \times 40'$. This field of view is achieved by a combination of four 512×512 pixels DEPFET (DEPleted Field Effect Transistor) devices, as shown in Figure 2.3. For very bright sources the WFI has a fifth sensor (only 64×64 pixels (Brand; 2017)) which can comprise the Fast Detector that is optimized for such sources and high count rates. In order to control all the DEPFETs, *Athena* has integrated circuits. These circuits are also able to read out the DEPFETs with detector electronics units that can perform on-board frame processing (Barret et al.; 2020).

2.3 The X-IFU

The X-IFU camera of *Athena* will provide X-ray spectroscopy with its hexagonal field of view of 5′ (diameter) with a spatial resolution of 2.5 eV up to 7 keV. The X-IFU is assembled of two cryogenic detectors. The primary one is made out of Molybdenum Gold transition edge sensors (Barret et al.; 2020). In general, transition edge sensors are made of a bolometer which has a thermally isolated absorber (Mauskopf; 2018). The absorbers of the X-IFU are composed of Gold and Bismuth (Barret et al.; 2020). These are then coupled to a superconducting thermometer. When the sensor absorbs a photon, it increases the temperature of the absorber which leads to an increase of the resistance of the superconductor. This causes a drop in the current, if the voltage is constant. These drops can then be read out as a signal. Transition edge sensors are widely spread in astronomical observations because of their low noise and high responsivity (Mauskopf; 2018). Because *Athena* will observe mostly weak and extended sources with the X-IFU it needs a second detector in order to assure a low background noise. This second detector will be below the focal plane of the primary one. With this technique it is possible to filter signals out that are not X-ray photons. If both detectors measure a signal at the same time, it will be removed. With this technique the X-IFU can filter out the non-X-ray signals because X-ray events exclusively reach the primary detector. All of this is only possible, when the system is cooled down to a very low temperature (< 100 mK) consistently. Otherwise the thermal noise would be too much (Barret et al.; 2020).

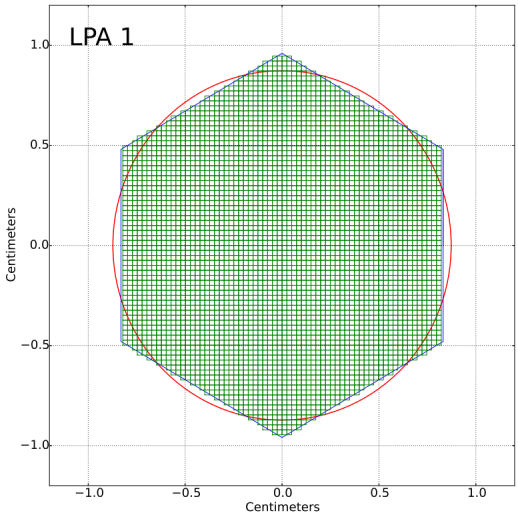

Figure 2.4: Image of the baseline configuration of the X-IFU. Image from Barret et al. (2016).

3 The Galactic Center

The Milky Way has a total diameter of about 30 kpc and is composed of several components. The solar system lies in the disk which is rotating with a velocity between 200 and 250 $\mathrm{km\,s^{-1}}$ and is made of spiral arms (see Figure 3.1). Towards the center lies a spherical structure of many old stars which is called the bulge. It extends to radii of 2 – 3 kpc. The bar is another structure of the central kiloparsecs in the Milky Way which is also composed of stars which rotate around the center on a cylindrical orbit. The structures which will be described in the following are located in the Central Molecular Zone (CMZ) (in the central few hundred parsecs). Within this region lies the Sgr A complex and its surroundings which will be the main focus of this thesis.

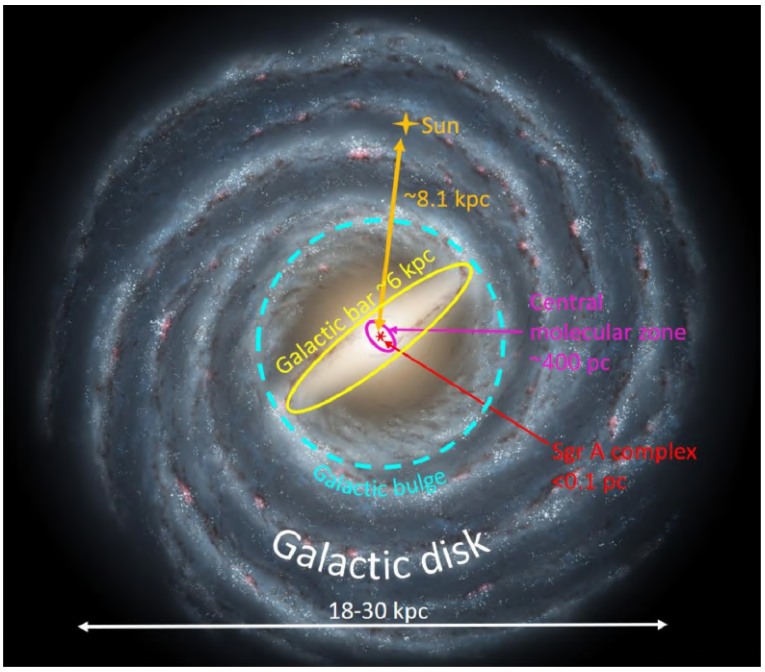

Figure 3.1: Illustration of the Milky Way with indications of the different components. Image from Bryant and Krabbe (2021).

3.1 The Central $\sim$ 400 pc

With an average molecular cloud H_2 volume density of $10^4\,\mathrm{cm^{-3}}$ (for comparison: $10^2\,\mathrm{cm^{-3}}$ in the disk) the CMZ is an extreme environment. This region lies inside the central few hundred parsecs of our galaxy and contains a massive stellar population (Bryant and Krabbe; 2021). Multiple dense and young star clusters have been discovered which are located within in the CMZ (Zwart et al.; 2002). The reason for the large stellar population in the surroundings of the GC are the clouds which represent a huge supply for the formation of stellar clusters. Because of that, around 10 % of all stars in the Milky Way

form in the GC ($0.07\,M_\odot\,yr^{-1}$ in the central 200 pc and $0.68-1.45\,M_\odot\,yr^{-1}$ in the entire disk of our galaxy). This correlation becomes even more apparent when looking at young and massive clusters (30 % are located in the GC) (Stolte; 2013). The three clusters with the most stars in them are the Arches, Quintuplet and Nuclear Stellar Cluster (NSC) (Bryant and Krabbe; 2021).
In order to show the structures and overall composition of the CMZ, a radio image of the central few hundred parsecs is shown in Figure 3.2.

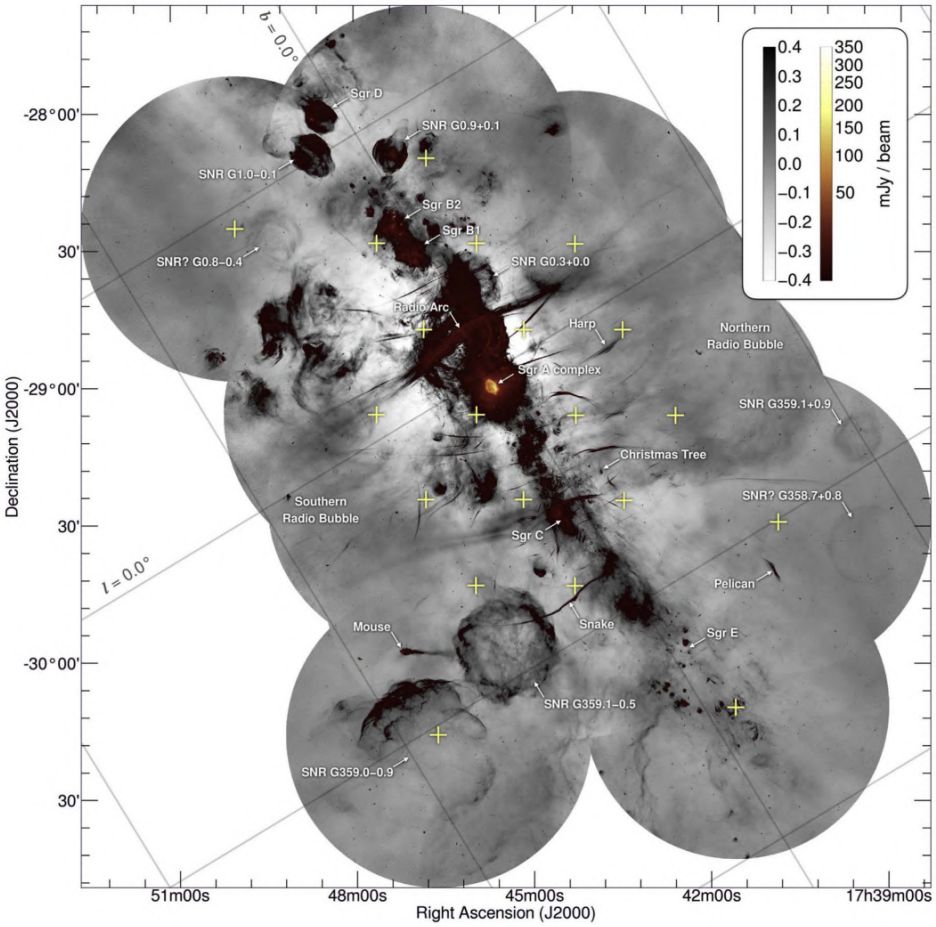

Figure 3.2: Radio image of the CMZ taken with MeerKAT which includes a total of 20 observations. It has dual color schemes with a gray scale for the faint end and a heat map for the bright end. It clearly shows the different Sgr complexes in this region where Sgr A in the center is by far the brightest radio source. It also detects several supernova remnants and numerous other radio features. Image from Heywood et al. (2022).

3.1.1 The Arches and Quintuplet Cluster

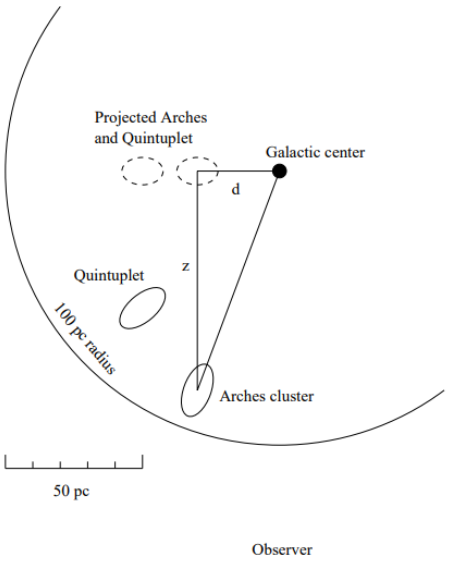

Figure 3.3: Schematic depiction of the location of the Arches and Quintuplet cluster with a projection from an observer. Image from Zwart et al. (2002).

About 26 pc east (in projection) of the GC lies the Arches cluster (angular distance to Sgr A*: $\sim 11.2'$). It is mainly made of massive stars (like O- and WR-type stars) which amount to a mass of $\sim 10^4\,M_\odot$. The age of the brightest stars among these is found to be about 2.5 Myr with older estimates as well. The dynamics of the Arches cluster is described by an almost circular orbit around the center (Bryant and Krabbe; 2021).
The Quintuplet cluster is located 4 pc further east in the projection (angular distance to Sgr A*: $\sim 13.0'$) and has the same radius (1 pc) and mass like the Arches cluster. The majority of its stars are likely O- and B-type stars which are slightly older than the ones from the Arches cluster (~ 4 Myr) (Bryant and Krabbe; 2021).
Because of their proximity and similarities, the clusters are likely to have formed from a similar event (if not from the same) with the Quintuplet cluster having an earlier origin (Bryant and Krabbe; 2021).

3.2 The Innermost Parsecs

Towards the central few parsecs of the Milky Way, the density of gas and stars increases even further. Around the very central object Sgr A* three main structures are located. These are on one hand gas structures like the Circumnuclear Disk (CND) and the Mini-Spiral (MS) and on the other hand the NSC. These objects are intimately related to each other and to Sgr A* in its dynamics and also their evolution (Bryant and Krabbe; 2021). For context, a radio image taken with MeerKAT is shown in Figure 3.4.

3.2.1 The Circumnuclear Disk

The CND extends from 1.5 – 5 pc around Sgr A* with a thickness of 0.3 – 0.4 pc and was found in infrared observations with the Kuiper Airbone Observatory. It has the shape of a flat torus with a cavity in the center where the MS and NSC are located. The CND is made out of neutral gas which is arranged in clumps with a volume density range of $10^{4-7}\,\mathrm{cm}^{-3}$. The major axis of this ring-structure is roughly aligned along the galactic plate and it is accompanied by filamentary features called "streamers" which connect the CND with its surroundings. A schematic image of this can be seen in Figure 3.5. These

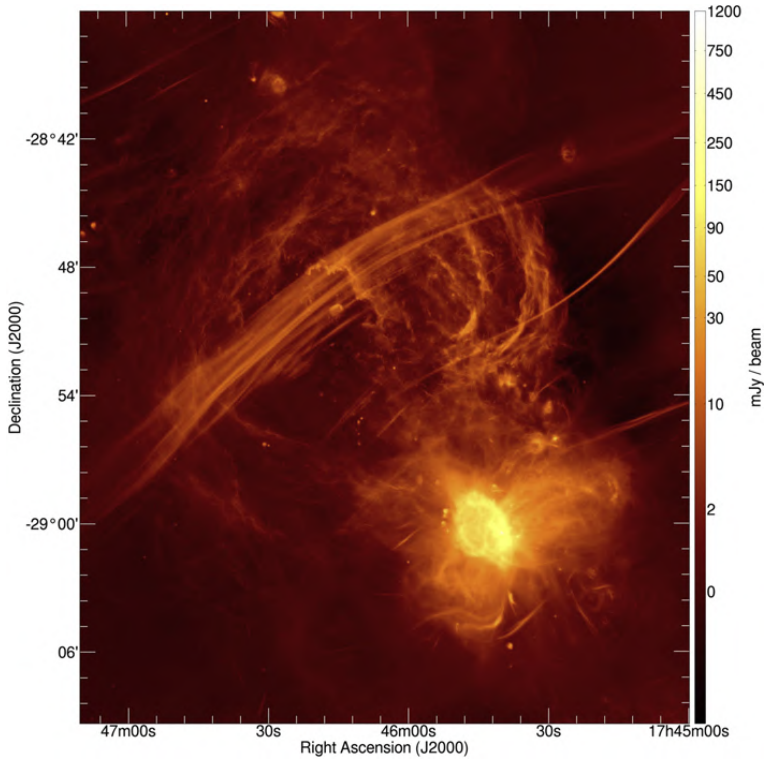

Figure 3.4: Radio image of Sgr A with a logarithmic heat map. It shows the luminosity of Sgr A* and its surroundings. Image from Heywood et al. (2022).

streamers represent a needed feeding mechanism for the disk because it steadily loses material to the more central objects. For such a feeding mechanism, the Eastern and Western Streamer provide the strongest case, where an interaction with the CND could have already been observed. As it stands now, the Northern Ridge is very questionable and the Southern Streamer has theoretically a high potential but no further evidence was found for that yet (Bryant and Krabbe; 2021).
As for the characterization of the gas in the CND, the estimates of mass and temperature vary a lot. This is the case because these depend significantly on the assumptions (geometric, chemical, thermodynamic) one makes and the tracers (Carbon-/Silicon-based or Hydrogen-based) one uses. These variations can be up to several orders of magnitude for the mass of the CND but a rough estimate is $\sim 10^4\,M_\odot$ and the temperature is in a range between 50 and 600 K. All in all, the CND marks the beginning for the very central parsecs in our galaxy and provides a gas and material flow towards the MS and NSC but also Sgr A* (Bryant and Krabbe; 2021).

3.2.2 The Mini-Spiral

In contrast to the CND, the MS is made out of ionized gas (H^+) and is composed of three separate arms. It has a diameter of around 2 pc and a mass of $60\,M_\odot$. The volume

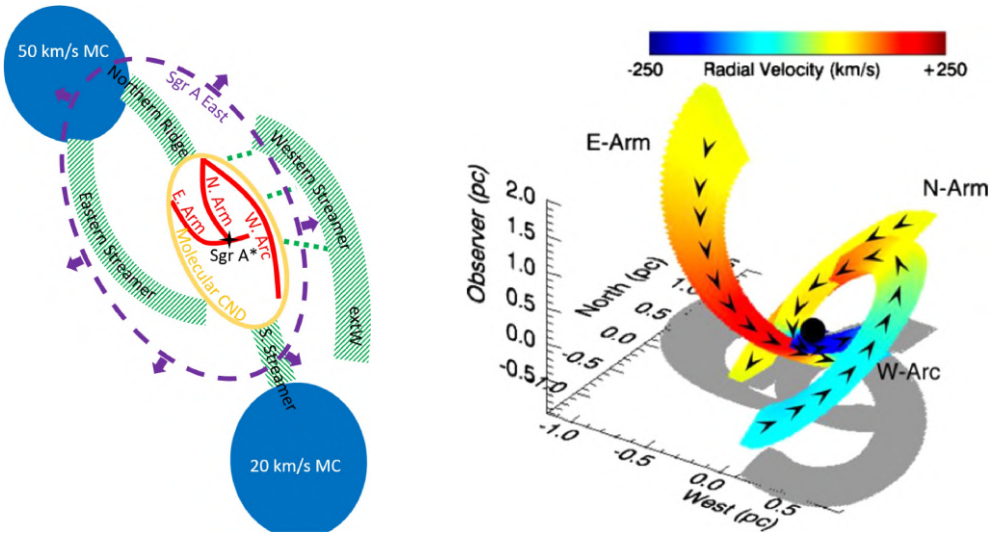

Figure 3.5: Left: Schematic overview of the CND and its surroundings. It is connected to molecular clouds (MC) with four different streamers. Within the CND is the MS located. Image from Bryant and Krabbe (2021).
Right: Schematic model of the MS with its three arms. The arrows represent the movement direction. Image from Zhao et al. (2010).

density is comparable to that in the CND but nevertheless the two objects are clearly spatially separated. First, the MS was found as a radio source which was then called Sgr A West. The spiral-structure was likely formed by the enormous tidal forces in that area. A model of the MS is depicted in Figure 3.5. All the three arms of the spiral are in constant motion in such a way that the Northern and Eastern Arm seem to collide into a central gas distribution which is called the "Bar". The majority of the gas in the MS forms a system of Keplerian orbits with just a few deviations. The orbits of the Northern and Eastern Arm are highly elliptical whereas the Western Arc has an almost circular orbit. Also with that movement, the MS provides an inflow of material towards Sgr A* of $\sim 3 \cdot 10^{-6}\,\mathrm{M_\odot yr^{-1}}$ (Bryant and Krabbe; 2021).

3.2.3 The Nuclear Stellar Cluster

The NSC is the stellar cluster which is located in the immediate surroundings of Sgr A* and numbers with the Arches and Quintuplet clusters to the brightest and most dense ($\sim 10^6\,\mathrm{M_\odot\,pc^{-3}}$) stellar populations within the central 100 pc. The first observations of the NSC were in the near- and middle-infrared spectrum and have shown that the cluster extends up to 5 pc around Sgr A*. It is worth mentioning that the NSC has a flattened shape along the galactic plane and not a perfectly spherical distribution (Bryant and Krabbe; 2021).

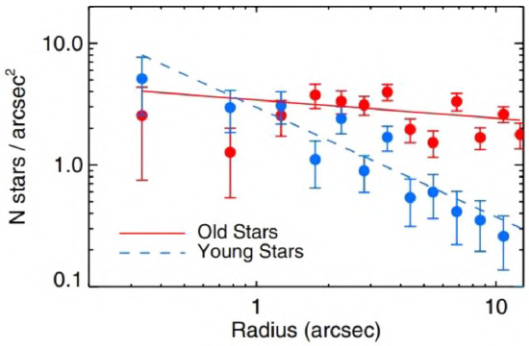

Figure 3.6: Density profile of the old and young stars in the GC. The young stars increase their number rapidly when getting closer to the center. Image from (Do et al.; 2013).

As for the characterization of the stars, about 80 % of all the stars in the central few hundred parsecs seem to be old stars ($> 5\,\mathrm{Gyr}$). Nevertheless there is still a significant proportion of younger stars located in the central parsecs. The distribution of the old and young stars depending on the distance to Sgr A* is shown in Figure 3.6. The metallicities of the old stars vary from subsolar to supersolar. Several of the old stars are observed to be red giants or even M class supergiants. The young stars on the other hand in the NSC amount to at least 100 with an age of just a few Myr. These are with a mass of $\sim 30\,\mathrm{M}_\odot$ mostly O, B, and WR giants. The stars that get the closest (1" or 0.04 pc) to Sgr A* are called the S-stars. These are defined by a strong cut-off in the density profile of the NSC and form a cluster of randomly oriented orbits. These stars are mainly B dwarf stars and are about $10-100\,\mathrm{Myr}$ old. The brightest star among these is the S2/S0-2 star (Bryant and Krabbe; 2021). S2 is on an elliptical orbit which gets very close to Sgr A* with a distance range of $130-1900\,\mathrm{AU}$ (Ghez et al.; 2003).

3.2.4 Sagittarius A*

By analyzing all the surroundings of the very center of the Milky Way, it is clear that there has to be a large central mass. It has a steady emission across the electromagnetic spectrum. It is most prominent as a radio source but also faint X-ray emission is detectable from it (as I present in the next chapter). The first estimation of its mass was done in the 1970s and 80s with observations of the dynamics of ionized gas. With that, the central mass amounts to $2-4\cdot 10^6\,\mathrm{M}_\odot$. After that, many calculations were made based on gas dynamics in the inner parsecs but these weren't completely convincing because gas can also be easily influenced by other effects than gravity. Consequently in the late 1980s and 90s the focus was on stellar observations around Sgr A* to strengthen the assumption of a central mass. As said, the S-stars (especially S2) are suitable for that (Genzel et al.; 2010). Ghez et al. (2003) provided with the orbit of S2 a direct measurement of the mass of Sgr A* ($4.1\,(\pm 0.6)\cdot 10^6\,\mathrm{M}_\odot$). With these calculations of S2 it was also possible to determine the kind of object Sgr A* is. It has to be an object with a minimum density of $5\cdot 10^{15}\,\mathrm{M}_\odot\,\mathrm{pc}^{-3}$ with a size of $< 1\,\mathrm{AU}$. When taking all of this knowledge together, Sgr A* has to be a supermassive black hole (Genzel et al.; 2010).

3.3 X-rays from the Galactic Center

The innermost parsecs of the Milky Way harbor many different objects which are also detectable as X-ray sources. The vicinity of Sgr A* is particularly X-ray luminous because of its many young and massive stars. A map of the X-ray emission from the central $8.4' \times 8.4'$ ($20\,\mathrm{pc} \times 20\,\mathrm{pc}$) is shown in Figure 3.7. The image shows that the X-ray

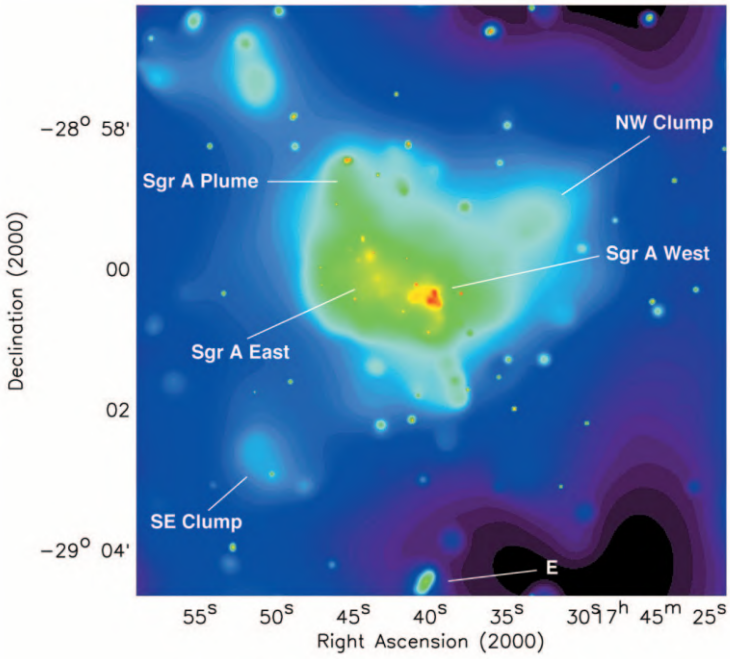

Figure 3.7: Smoothed and flat-fielded image of the central $8.4' \times 8.4'$ of the Milky Way in the $0.5-7\,\mathrm{keV}$ band from *Chandra*. Image from Baganoff et al. (2003).

emission in the central parsecs rises towards the vicinity of Sgr A* (the red region). It is also noticeable that X-ray emitting hot plasma is widespread in the central $\sim 10\,\mathrm{pc}$ which gets a lot more concentrated towards the central parsec (yellow in Figure 3.7). The CND is not evident in the X-ray observations but might as well influence the X-ray emission in this region. It possibly confines the hot plasma because the western side of the X-ray emission in the central parsec has a very similar shape to the Western Arc of the MS (Sgr A West). Sgr A* itself is also an X-ray source (ca. $1.3\,\mathrm{erg\,cm^{-2}\,s^{-1}}$ in the $2-10\,\mathrm{keV}$ band) likely because of accretion onto the black hole with thermal and nonthermal emission components. More eastern, another strong X-ray source can be found which is called Sgr A East and is interpreted as a supernova remnant. *Chandra* also discovered two bright clumps (NW and SE clump) which are located on either side of the Galactic plane. These have strong emission in the soft band under 6 keV while Sgr A East dominates the harder band above that value (Baganoff et al.; 2003).
Further away from Sgr A* the X-ray luminosity decreases. The distribution of the X-ray population in the central few hundred parsecs is shown in Figure 3.8. The $\log N - \log S$

on the left indicates the number of sources N per deg^2 that have a higher flux than S_0 dependent on S_0. It shows that the number of sources above a given flux is permanently higher in regions closer to the center than in those further away. The same trend is shown on the right in the image. Here, the number of sources per deg^2 is plotted as a function of the angular distance from the center. It displays a decrease in the X-ray population with the distance to the GC. This decrease is partly explained by the decline of the stellar population (green) but towards Sgr A* the X-ray population is even more concentrated than the stars (Hong et al.; 2009).

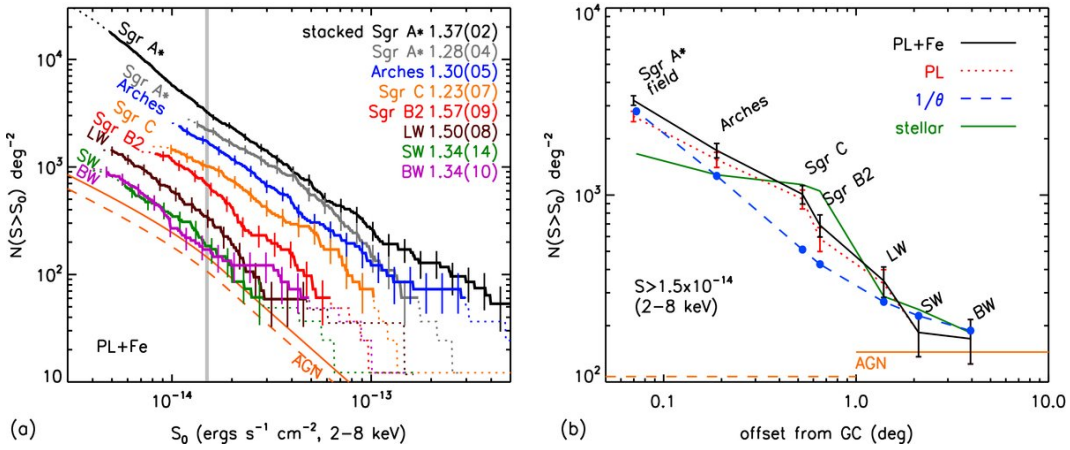

Figure 3.8: Left: $\log N - \log S$ distribution of the X-ray population in the GC of different regions. Right: Radial distribution of the X-ray population (with fluxes higher than the indicated S_0 in gray on the left) in the GC. PL+Fe means that a power law plus an iron emission line was used as a spectral model. Image from Hong et al. (2009).

4 X-Ray Sources

In this chapter, I will present an overview of stars and X-ray binaries as X-ray sources and their emission origins.

4.1 Stars

Almost every star type of the Hertzsprung–Russell diagram is very prominent as an X-ray source (see Figure 4.1). The X-ray emission depends heavily on the type of the stars and other properties that can be studied with their X-ray spectra. Because of that, stars are among the most important X-ray emitters (Güdel and Nazé; 2009).

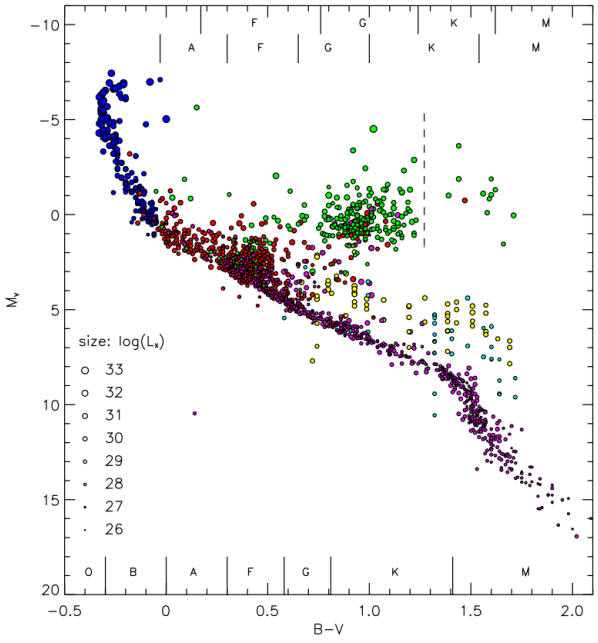

Figure 4.1: Hertzsprung-Russell diagram of 2000 stars which are detected as X-ray sources. It shows that stars are X-ray emitters throughout all spectral classes, including the pre-main sequence, main-sequence, giants and supergiants. Image from Güdel (2004).

4.1.1 Cool Stars

Cooler stars (type F to M) have a very high magnetic activity. Like the sun, they have coronae which is caused by a dynamo which generates strong magnetic fields. The dynamo is present in these cool stars because of an interaction between the rotation and the convection. Due to the magnetic fields, gas gets trapped and heated which then sends out thermal radiation in the X-ray band. Apart from the thermal X-ray emission, cool stars also show X-ray flares. These flares are observable throughout the electromagnetic

spectrum and are caused by an abrupt release of energy from the magnetic fields in the corona. Typically, they increase the radiation within few minutes to hours up to a peak and then decay within several hours (Güdel and Nazé; 2009).
The X-ray luminosity (L_{X}) of cool stars is correlated to the rotation as well as the coronal temperature. The relation to the rotation period P is:

$$L_{\mathrm{X}} \propto P^{-2}. \tag{1}$$

This effect has a saturation at about $L_{\mathrm{X}} \sim 10^{-3}\, L_{\mathrm{bol}}$ (with the bolometric luminosity L_{bol}) where a further increase of the rotation speed doesn't increase the luminosity. The rough connection to the coronal temperature T is as follows:

$$L_{\mathrm{X}} \propto T^{4.5\pm0.3}. \tag{2}$$

In Figure 4.2 two spectra of cool stars, which are solar analogs, are shown to present the correlation between X-ray emission, the age and the coronal temperatures. The younger, hotter one has clearly a higher activity with respective larger fluxes. This confirms the correlation between these parameters and shows that generally older stars have a lower coronal temperature and therefore a lower X-ray luminosity (Güdel and Nazé; 2009).

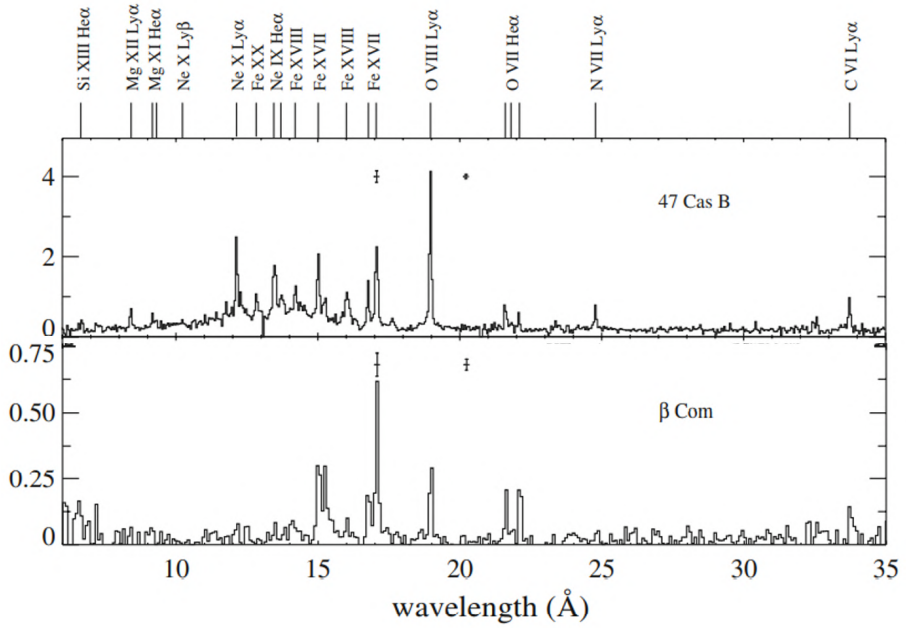

Figure 4.2: X-ray spectra of two solar analogs from XMM-Newton. Top: Younger star with a higher activity and coronal temperature. Bottom: Older star with a lower activity and coronal temperature. x-axis is the wavelength [Å], y-axis is the flux [10^{-3} photons cm^{-2} s^{-1} Å^{-1}]. Image from Güdel and Nazé (2009).

4.1.2 Young Stars

Before stars enter the main-sequence, they are also X-ray sources. As a "class 0" protostar, most of the mass which will later form the star is still located in a molecular envelope (Güdel; 2004). For these protostars no definite X-ray observations were made so far (Güdel and Nazé; 2009). After this stage, the star is a "class I" protostar where they already have accreted most of their final mass but they are still surrounded by a circumstellar disk (Güdel; 2004). These protostars have been detected as X-ray emitters where the characteristics of the spectrum is similar to the T Tauri star (TTS), which is the latest stage in star formation, which verifies the presence of a magnetic corona in the pre-main sequence. They also show X-ray flares, which is typical for their descendants (TTS) as well (Güdel and Nazé; 2009). There are different types of TTS. A "classical T Tauri" (CTTS or "class II") still has a circumstellar disk in its surroundings while the "weak-lined T Tauri" (WTTS or "class III") lost most of the disk. The CTTS are recognizable by the intense Hα emission line in their spectrum which the WTTS barely has (Güdel; 2004). Two example spectra are shown in Figure 4.3.

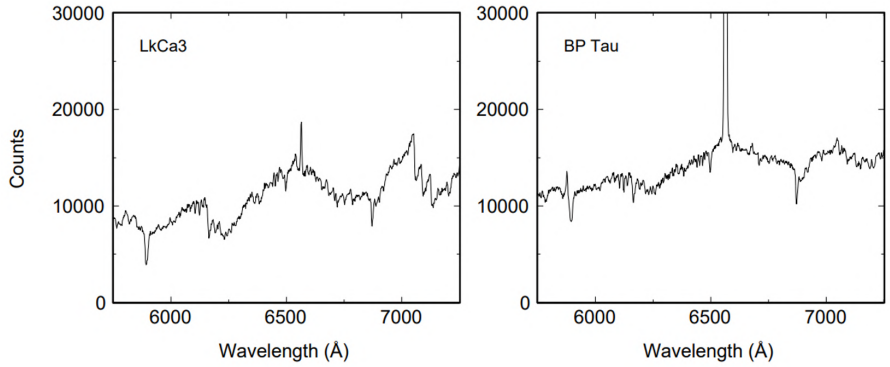

Figure 4.3: Optical spectra of two TTS. A WTTS on the left and a CTTS with an excess Hα emission line on the right. Image from Kenyon et al. (1998).

On average, WTTS are observed to have a higher X-ray luminosity than CTTS, although most of pre-main sequence stars are saturated because of their short rotation period. Their saturation is at about $L_{\mathrm{X}} \sim 10^{-3.5}\, L_{\mathrm{bol}}$ which is slightly different to the late-type main-sequence stars. The correlation to the age is that at about 1 Myr the X-ray luminosity peaks and after that it gradually declines due to loss of angular momentum (Güdel and Nazé; 2009).

4.1.3 Hot Stars

The most massive, most luminous and hottest stars in the Hertzsprung–Russell diagram are the O- and early B-type stars. They all have a very high mass-loss rate which results in a strong stellar wind ($10^{-6}\,\mathrm{M}_{\odot}\,\mathrm{yr}^{-1}$). These massive stars have already been discovered 30 years ago as X-ray emitters. Their spectra usually appear thermal and contain discrete

emission lines from metals. Single hot stars rather emit in the soft band where the main components have temperatures less than 1 keV. One example for a spectrum of a B star is shown on Figure 4.4 (Güdel and Nazé; 2009).

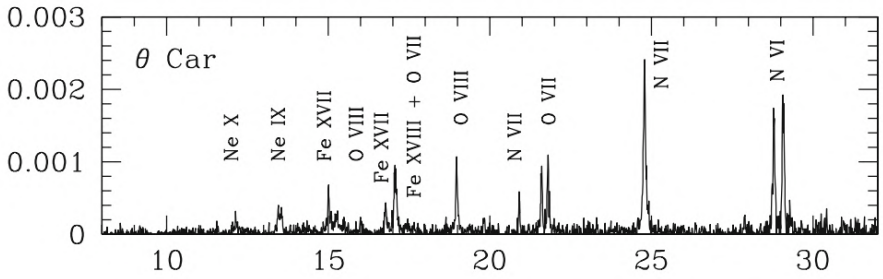

Figure 4.4: X-ray spectrum of the B-type star θ Car with indications of the metals of the discrete emission peaks. x-axis is the wavelength [Å], y-axis is the flux [counts $\mathrm{cm}^{-2}\,\mathrm{s}^{-1}\,\mathrm{Å}^{-1}$]. Image from Güdel and Nazé (2009).

The origin of the X-ray emission from hot stars are most likely shocks in their winds. These arise because of the varying velocity in an unstable wind. The slower material gets passed by the fast-moving material which causes shocks between them (Güdel and Nazé; 2009). First, forward shocks in the wind were considered the most likely origin of X-ray emission (Lucy and White; 1980). Later, the generation of dense shells in the wind which collide with each other was proposed as a probable cause of X-rays as well (Feldmeier et al.; 1997). Generally, if two hot stars form a binary system, they appear brighter and harder in the spectrum than a single source because of the interaction between the winds of the two objects (Güdel and Nazé; 2009).

4.1.4 Wolf-Rayet Stars

O stars are the ancestors of Wolf-Rayet (WR) stars of which there are three different types: WN, WC and WO (letters refer to the element which dominates the spectrum: nitrogen, carbon or oxygen). These stars have much denser winds (especially WC) and an about ten times higher mass-loss rate than O stars. So far, WC stars are undetected in the X-ray energy band which may be caused by the fact that the emission happens deep in the wind which results in a complete absorption. On the other hand, several WN stars are clearly detected as X-ray sources but there is a wide variety in the properties of them. Therefore, individual modeling of the spectra is necessary and there are still some undetected ones. Only one very faint WO star has been observed as an X-ray source but its faintness prevented any spectral analysis. The only conclusion from this observation is a high temperature of the source which can't be explained by shocks in the wind. Most of the detected WR stars are binary systems which is caused by the same effect that the wind-wind interaction results in a brighter X-ray emission (Güdel and Nazé; 2009).

4.2 X-Ray Binaries

X-ray binaries are among the brightest X-ray sources in our galaxy with fluxes well over $10^{-10}\,\mathrm{erg\,cm^{-2}\,s^{-1}}$ in the $1-10\,\mathrm{keV}$ band (Tauris and Van Den Heuvel; 2006). Generally they consist of two objects. One compact object which is the gainer and one normal star which is the donor. The X-ray binaries can be classified by the mass of the donor (high-mass/low-mass X-ray binaries) or their compact companion (black-hole systems, neutron star X-ray binaries or cataclysmic variables for white dwarfs). High-mass X-ray binaries (HMXBs) consist of an early-type star with type O or B whereas low-mass X-ray binaries (LMXBs) contain a star with spectral type of A or later (Reig; 2011).
X-rays from HMXBs are produced by the strong stellar wind of the stellar companion. This stellar wind gets partly captured by the compact object and is sufficient to power a bright X-ray source for up to a million years (see Figure 4.5). HMXBs with neutron stars have X-ray spectra of over 15 keV and often show regular pulsations in their X-ray emission. LMXBs don't emit their X-rays because of the stellar wind from the companion but because of a mass transfer. This mass transfer works with Roche-lobe overflow where the majority of the matter gets to the compact object via an accretion disk (see Figure 4.5). The spectra of LMXBs are softer with an energy of under 10 keV and only a few of them have pulsations but often X-ray bursts. This is due to the fact that the neutron star of a LMXB often has weak magnetic fields compared to those in a HMXB because of the age difference (neutron stars in HMXBs are several orders of magnitude younger and therefore have a stronger magnetic field). For an X-ray pulsar a strong magnetic field is needed whereas for the bursts a weak one is required (Tauris and Van Den Heuvel; 2006).

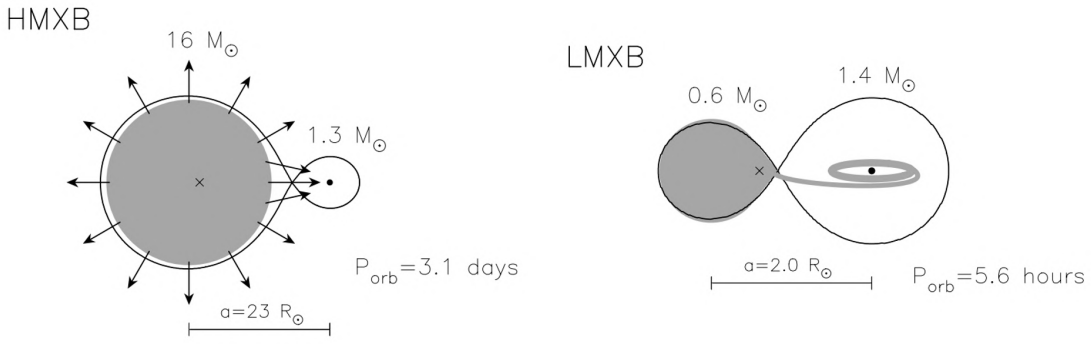

Figure 4.5: Examples of typical X-ray binaries. Left: HMXB where the compact object is mainly fed by the strong stellar wind of its companion. Right: LMXB where the compact object is fed via an accretion disk by Roche-lobe overflow. Image from Tauris and Van Den Heuvel (2006).

The distribution of X-ray binaries in the Milky Way is shown in Figure 4.6. It shows that the HMXBs are concentrated towards the galactic plane while the LMXBs accumulate mainly towards the GC (Grimm et al.; 2003). This is the reason why I will later encounter two LMXBs in my simulations of the GC.

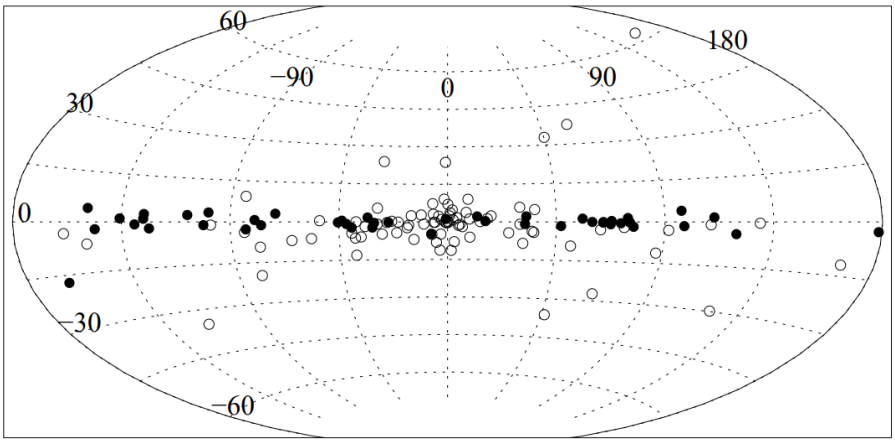

Figure 4.6: Distribution of X-ray binaries in the Galaxy. A total of 86 LMXBs (open circles) and 52 HMXBs (filled circles) are shown. Image from Grimm et al. (2003).

5 SIXTE

The simulation software which will be used is called SIXTE (SImulation of X-ray TElescopes) and is a Monte Carlo-based toolkit. With SIXTE it is possible to perform mission-independent simulations for X-ray instruments. It focuses on very detailed modeling of the detectors of an X-ray telescope. Because of these features SIXTE is well suited for simulations for the WFI and X-IFU of *Athena* (Dauser et al.; 2019).
The process of a SIXTE simulation is schematically shown in Figure 5.1. First, the information of the chosen sources have to be assembled in an input file called SIMPUT. With this catalogue of sources the software generates photons that interact with a representation of the instruments of the mission to get an impact list (impact times, positions, and energies). For the photon generation it is important to enter the effective area, field of view and pointing direction of the telescope. Then, only photons that will hit the instrument will be generated. Lastly, an event list is created by applying the impact list on the detector model which is based on its detailed specifications (Dauser et al.; 2019).

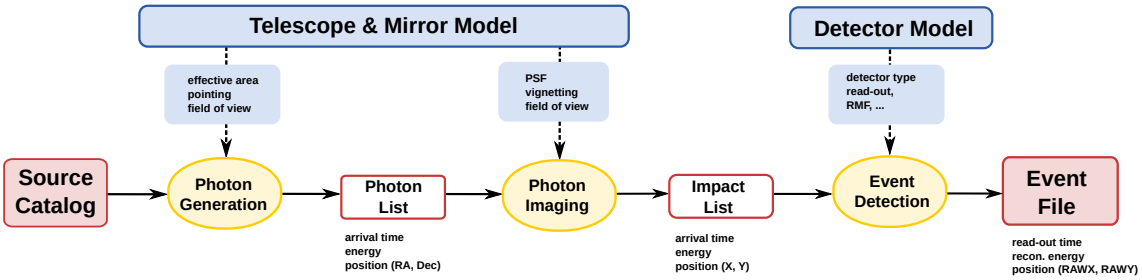

Figure 5.1: Schematic process of a simulation with SIXTE. Starting left with the generation of photons of a source catalog. These photons are then detected and imaged by the chosen instrument and generate an impact list. In the end on the right, these events are processed and generate an event list (Dauser et al.; 2019).

5.1 SIMPUT

The SIMPUT file is a FITS-based format and contains all the necessary properties of a source (catalog) for the simulation. These include the basic information like position (right ascension and declination) and the flux in a specific energy band in the main extension. Several extensions can be added for further detailed modelling. With the photon flux density distribution (photons $\mathrm{cm}^{-2}\,\mathrm{s}^{-1}\,\mathrm{keV}^{-1}$) of a source it is possible to add the spectrum to the SIMPUT file. If the observed source is also time dependant, one can use the light curve, power spectral density or photon list (depending on the time for each photon) to consider the time variability. Images of the used sources can also be included in an additional extension. The corresponding tool to create a SIMPUT file is called `simputfile` (Dauser et al.; 2019). The necessary arguments for a SIMPUT for a simulation are shown in Table 1.

Table 1: Listing of the required parameters for a simulation input file for a simulation with SIXTE.

Parameter	Explanation
`SRC_ID`	Number for source identification
`RA`	Right ascension [°]
`DEC`	Declination [°]
`E_MIN`	Lower bound for energy band [keV]
`E_MAX`	Upper bound for energy band [keV]
`FLUX`	Flux of the source in the energy band [$\mathrm{erg\,cm^{-2}\,s^{-1}}$]
`SPECTRUM`	Reference to spectrum (in separate extension or file)

5.2 *Athena* Tools

The two main simulation tools which will be used in this thesis are `athenawfisim` (for the WFI) and `xifupipeline` (for the X-IFU).
`athenawfisim` requires for a simulation four XML files which store the information of one WFI chip each. The other necessary parameters are right ascension and declination (or an attitude file with the pointing dependent on time) of telescope pointing, the used SIMPUT file and the exposure time in seconds. The output of this simulation tool is four event files (one for each chip) which then need to be merged together in order to receive the entire image of the WFI.
For simulations with the X-IFU, two XML files are essential. One with basic information of the detector and another with advanced definition. The parameters for the pointing direction as well as the SIMPUT file and exposure time are the same as for the WFI.

For further information and description of the features of SIXTE one can download the manual[2].

[2] `https://www.sternwarte.uni-erlangen.de/~sixte/data/simulator_manual_v1.3.16.pdf`

6 The Source Catalog

The source catalog which will be used for the simulations is from Muno et al. (2009). It includes 9017 sources within a $2^\circ \times 0.8^\circ$ field around the GC that were detected in *Chandra* observations. The data were taken in the early and mid 2000s and include a total of 88 *Chandra* observations with a total exposure time of 2.25 Ms. A plot of all the sources in this catalog is shown in Figure 6.1. It is noticeable that the sources are irregularly distributed which is caused by the different exposure times of the fields. Therefore, a flux limited map with a more even distribution is also shown in Figure 6.1. The catalog can be downloaded from the VizieR archive server of the CDS[3].
The data of the catalog which were used to build a SIMPUT file for the simulations are summarized in Table 2.

Table 2: Listing of the used data columns of the catalog (Muno et al.; 2009).

Parameter	**Explanation**
`RAJ2000`	Right ascension (J2000) [°]
`DEJ2000`	Declination (J2000) [°]
`Exp`	Exposure time [s]
`Sct.net`	Net counts 0.5 – 2.0 keV in source region
`l_Sct.net`	Limit flag on 0.5 – 2.0 keV net counts
`Hct.net`	Net counts 2.0 – 8.0 keV in source region
`l_Hct.net`	Limit flag on 2.0 – 8.0 keV net counts
`Sflux`	Photon flux 0.5 – 2.0 keV [photons $\mathrm{cm}^{-2}\,\mathrm{s}^{-1}$]
`Hflux`	Photon flux 2.0 – 8.0 keV [photons $\mathrm{cm}^{-2}\,\mathrm{s}^{-1}$]

The "limit flag" indicates a non-detection at the 90 % confidence level for the respective energy band of the net counts (Muno et al.; 2009). For the following simulations the count rate was always set to zero if the respective limit flag was given. This results in 1927 sources with counts in both bands, 5825 sources exclusively in the hard band, 1127 sources exclusively in the soft band and 138 sources with no counts.
In order to obtain the flux of the sources ($\mathrm{erg}\,\mathrm{cm}^{-2}\,\mathrm{s}^{-1}$) the resulting counts needed to be converted. For that, the count rate was calculated by dividing the net counts by the exposure time. These count rates were multiplied by a conversion factor, which was calculated with the HEASARC tool[4]. Throughout all the simulations a hydrogen column density of $N_\mathrm{H} = 14.3 \cdot 10^{22}\,\mathrm{cm}^{-2}$ (Mossoux et al.; 2020) was used.

[3] `http://cdsarc.cds.unistra.fr/viz-bin/VizieR-3?-source=J/ApJS/181/110/catalog`
[4] `https://heasarc.gsfc.nasa.gov/cgi-bin/Tools/w3pimms/w3pimms.pl`

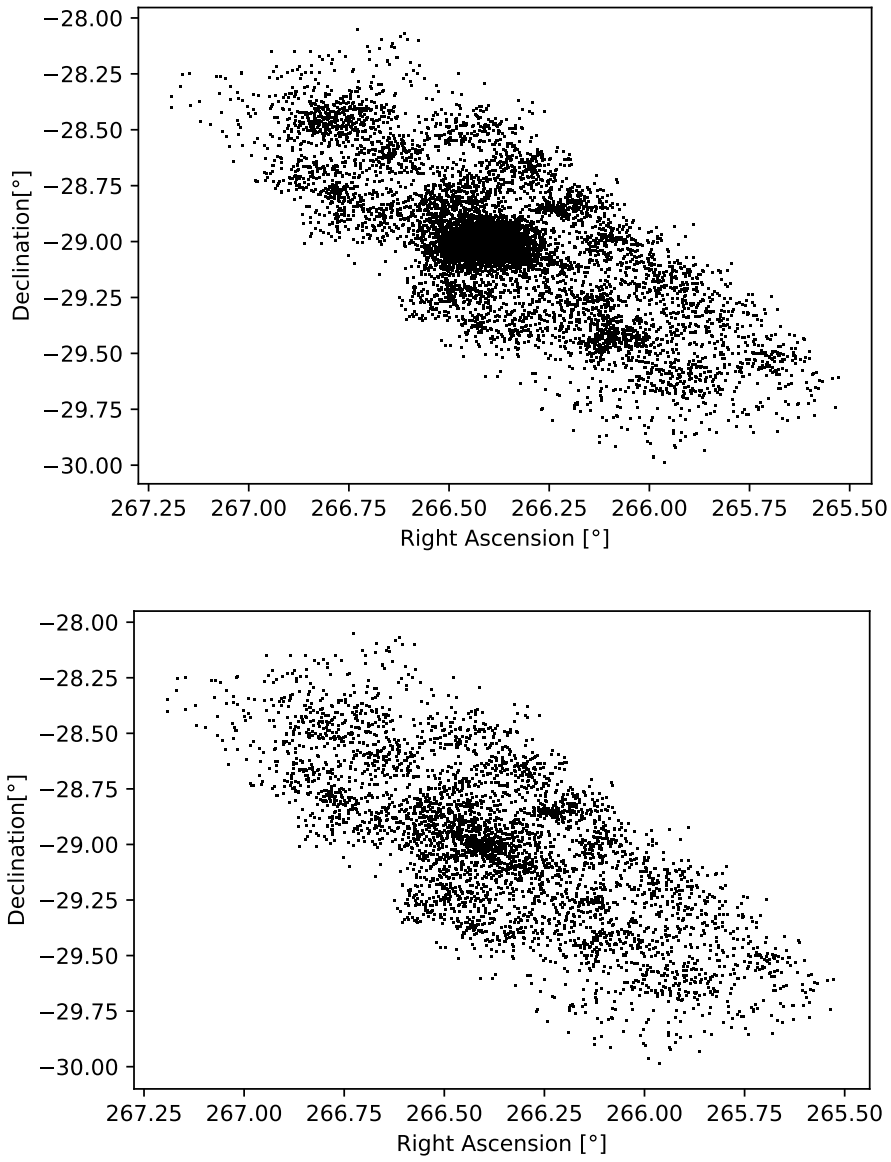

Figure 6.1: Top: Plot of all the sources in the catalog as dots with right ascension and declination in degrees as axes with an irregular distribution due to varying exposure times.
Bottom: Plot of the sources with a photon flux of over $5 \cdot 10^{-7}$ photons $\mathrm{cm}^{-2}\,\mathrm{s}^{-1}$ in the $0.5-8.0\,\mathrm{keV}$ band (4339 in total) with a more even distribution.

7 The Simulations

7.1 First WFI Simulation

For the first simulation the spectral shape of all sources was set to the same model. This spectrum is an absorbed power law with a photon index of 2.2 (so a rather soft spectrum). `isis`[5] was used to create a parameter file for the `simputfile` tool. The factor to convert the count rates into a flux, calculated by the HEASARC tool, is 2.733^{-11} erg cm^{-2} in the 0.5 – 8 keV band.
In order to cover the gaps between the sensors of the WFI a time-varying pointing of the telescope must be specified. This was done with an attitude file which was created with the `attgen_dither` tool. This creates a Lissajous pattern for the given parameters. These were an amplitude of 0.03° and an exposure time of 100 ks. The center of the dithering was set to a position slightly more north and east than Sgr A* in order to get a higher exposure time of the very center of the galaxy.

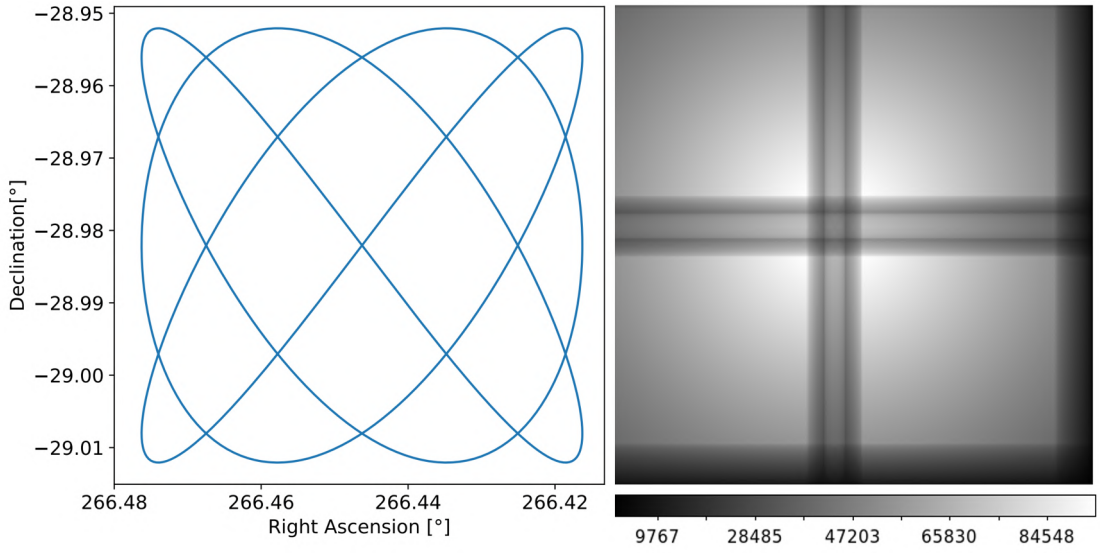

Figure 7.1: Left: Plot of the pointing position from the attitude file. Right: Image of the exposure map of the WFI with a Lissajous pattern and the slightly shifted pointing (scale indicates exposure time in seconds).

The four resulting event files from `athenawfisim` were merged together with `ftmerge`. To generate an image out of that `imgev` was used (the arguments of the pixels and spatial resolution were set to match the WFI). The parameters for the pointing of the map were set to Sgr A* in order to place it in the center. The last step was to correct the exposure of the image with an exposure map (see Figure 7.1) from the `exposure_map` tool. In order to scale the simulated image from counts to counts per second, it was divided by the exposure map in `isis`. The final image of the simulation for the WFI is shown in

[5] `https://space.mit.edu/asc/isis/`

Figure 7.2. All images in this thesis were processed and displayed with `ds9`[6].

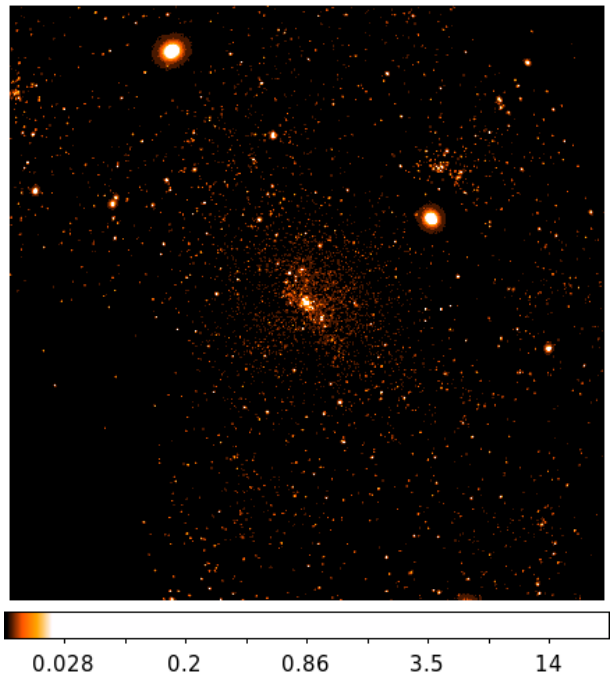

Figure 7.2: Final image of the first simulation of the GC with the WFI and an exposure time of 100 ks (scale displays counts per second).

It is noticeable that the sources, which were simulated as point sources, look like an extended emission. Also, three bright parts are especially prominent. These are on one hand as expected Sgr A* and its immediate surroundings in the center as well as two very bright sources (one in north-east and one in the north-west of Sgr A*) on the other hand. Both of them are likely LMXBs (Hong et al.; 2016). The one in the north-east (so top left in the image) is 1E 1743.1−2843 and the other one is GRS 1741.9−2853. The nature of the compact object of 1E 1743.1−2843 is unclear until today but the spectrum indicates that a neutron star is most likely (Raman et al.; 2018). It shows no periodic pulsations and was the brightest source in the 3.0 − 40.0 keV band from the *NuSTAR* observations of the GC (Hong et al.; 2016). GRS 1741.9−2853 is because of its many type-I X-ray outbursts a neutron star LMXB (Pike et al.; 2021).
In the image of the GC with the WFI is only a part of all 9017 sources from the catalog present because of its restricted field of view. Within the image lie 6201 sources in the catalog, so about two-thirds. A depiction of the covered area from the WFI with all four chips of the catalog is shown in Figure 7.3. This image also explains why the south-east corner of the simulation is mostly empty because the catalog does not have many sources in this region.

[6] `https://ds9.si.edu`

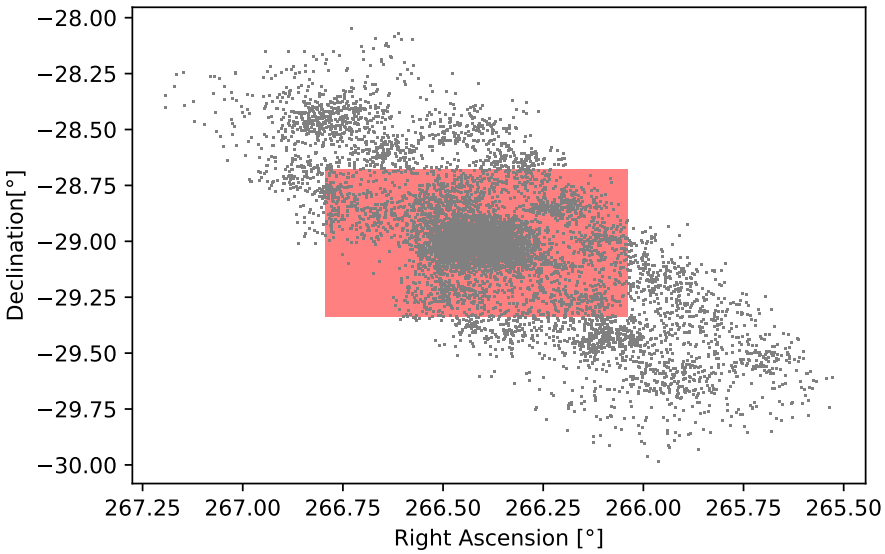

Figure 7.3: Plot of all the sources in the catalog as dots with the covered area from the WFI in red.

7.2 Improving the WFI Simulation

In order to improve the simulation and make it more realistic, the sources need to have assigned an individual spectrum which describes them best. For that, the `Sflux` and `Hflux` of the catalog were used to calculate a Hardness Ratio (HR) for the 1927 sources with an X-ray emission in both energy bands:

$$\mathrm{HR} = \frac{\texttt{Sflux}}{\texttt{Hflux}} \tag{3}$$

The model which was used for these sources is an absorbed thermal bremsstrahlung model. This spectral model was utilized because many sources can be described with a bremsstrahlung or comptonization spectrum. Both generate spectra that have roughly the shape of

$$E^{-\Gamma} \cdot \exp\left(-\frac{E}{E_{\mathrm{fold}}}\right). \tag{4}$$

For bremsstrahlung E_{fold} is the `kT` value. Because of that, the difference to the normal power law is especially important for harder spectra.
In order to match the HR of each source to a `kT` value for the model, the `flux` tool from `Xspec`[7] was utilized. For 27 different `kT` values in an interval between 0.065 and 2.0 keV (all 1927 sources lie within this range) the respective HR was calculated with Equation 3. These points were plotted and then linearly interpolated. This is shown in Figure 7.4.

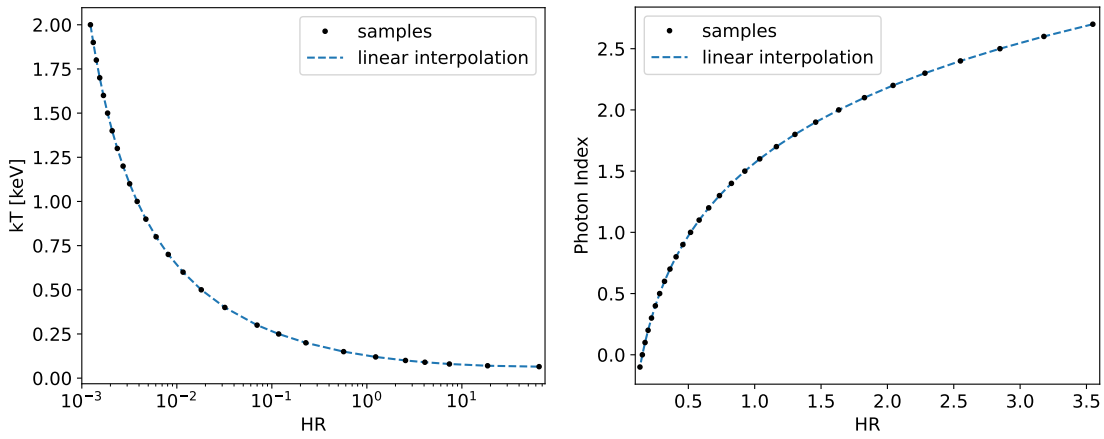

Figure 7.4: Left: Interpolated function for `kT` for the HR (soft: 0.5 – 2.0 keV hard: 2.0 – 8.0 keV) from the *Chandra* catalog. Right: Interpolated function for the photon index for the HR (soft: 3.0 – 10.0 keV hard: 10.0 – 40.0 keV) from the *NuSTAR* catalog.

After that, a total of 96 spectra in the range of 0.065 to 1.9 keV were generated and put into the SIMPUT file. The step width between two consecutive `kT` values gets smaller towards 0.065 keV. With the interpolated function and the HR of every source, `kT` was

[7] `https://heasarc.gsfc.nasa.gov/xanadu/xspec/`

computed for each one. Then, every source was assigned to the spectrum which is closest to its HR.
For the 1127 sources which only have a flux in the soft band (0.5 – 2.0 keV), the median of all the `kT` values from the sources with emission in both bands was used, i.e., 0.187 keV. Then, a spectrum with `kT` = 0.187 keV was added to the SIMPUT and all 1127 sources were assigned to that spectrum.
In order to get a spectrum for the 5825 sources which were only detected in the 2.0 – 8.0 keV band, a *NuSTAR* catalog from Hong et al. (2016) of the GC was used (it is also available on the VizieR archive server[8]). It includes 70 sources with emission in the 3.0 – 79 keV energy band. Out of these 70 sources, 41 have exclusively an emission in the 2.0 – 8.0 keV band in the *Chandra* catalog. For these sources, an absorbed power law was used as a spectral model. A selection of photon indices dependant on the HR (now the soft flux is in 3 – 10 keV and the hard flux in 10 – 40 keV; fluxes came from the *NuSTAR* catalog) was calculated with the `flux` tool from `Xspec` and an interpolation was done (see Figure 7.4 on the right). With the interpolated function the photon index of each of the 41 sources was computed. The median photon index of 1.51 was used as a spectrum for the 5825 hard sources from the *Chandra* catalog.
The temperature distribution of the 1927 sources with detection in both bands from the *Chandra* catalog and the distribution of the photon index of the 41 hard sources from the *NuSTAR* catalog are shown in Figure 7.5.

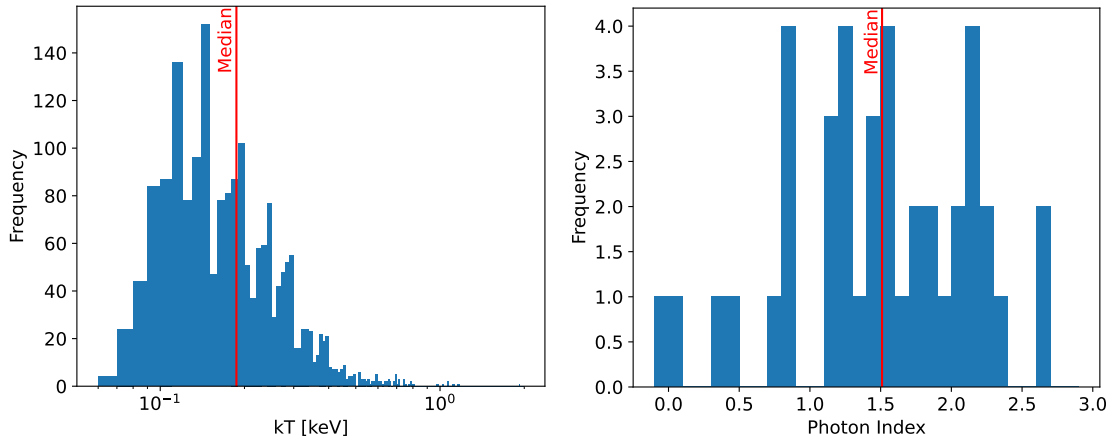

Figure 7.5: Left: Histogram of the temperature distribution of the 1927 sources from *Chandra* which were modeled with an absorbed bremsstrahlung. Right: Histogram of the distribution of the photon index for the 41 sources from *NuSTAR* which were modeled with an absorbed power law.

The factor to convert the count rate into the flux in the 0.5 – 8.0 keV band was again calculated with the HEASARC tool. Each source count rate was multiplied by the respective factor of the spectral model it was assigned to. For the simulation process, the

[8] `https://vizier.cds.unistra.fr/viz-bin/VizieR-3?-source=J/ApJ/825/132/table24`

same steps with the same parameters as before were done. This includes the dithering, exposure time, image generation and exposure correction. The final image of the simulation with the improved SIMPUT is shown in Figure 7.6.

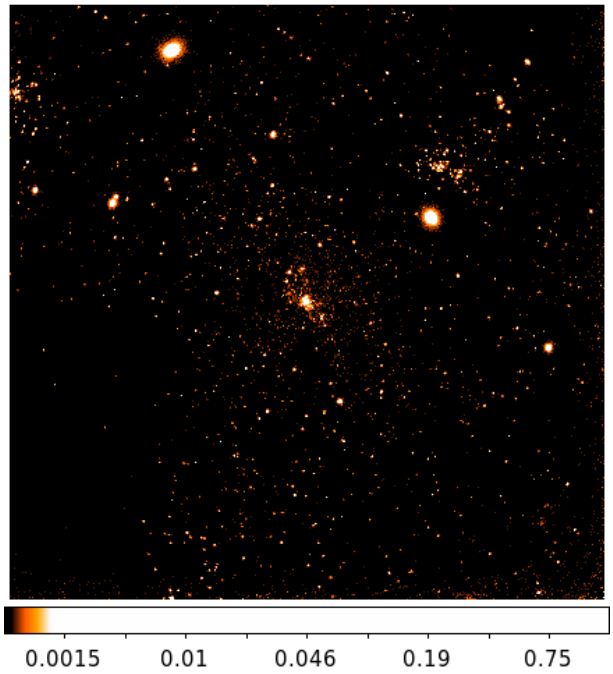

Figure 7.6: Image of the improved simulation of the GC with the WFI and an exposure time of 100 ks (scale shows counts per second, displayed with `ds9`).

When comparing this image to the first simulation, they seem pretty similar. But at second glance, the differences are noticeable. In this image, there is a larger variability throughout the sources. With the first simulation almost all sources looked the same and just varied in their brightness and spreading. Now the adjusted spectra influence the final image and make it more realistic.

7.3 X-IFU Simulation

After the simulations with the WFI, also one with the X-IFU was done. The SIMPUT for that was the same as in the last chapter, so the improved one with individual spectra. For the simulation the `xifupipeline` tool was used. The exposure time was set to 100 ks and the pointing directly to Sgr A*. The image was created with `imgev` and the parameters were set to match the setup of the X-IFU. The final image can be seen in Figure 7.7.

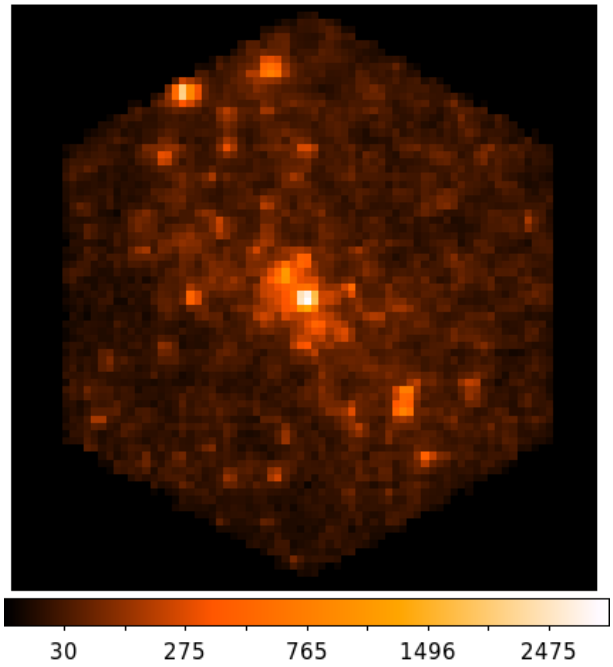

Figure 7.7: Image of the simulation of the GC with the X-IFU and an exposure time of 100 ks (scale indicates counts, displayed with `ds9`).

Because of the much smaller field of view of the X-IFU compared to the WFI, the only noticeable source is Sgr A* and its immediate surroundings in the center. As expected, the image quality is much worse than with the WFI. This is caused by the fact that the X-IFU has far less and larger pixels than the WFI, because it is made for spectroscopy and less well suited to imaging (Barret et al.; 2020).

7.4 RGB Image

In order to get a better understanding of the sources and in which energy band they emit X-rays, an RGB image of the GC with the WFI was made. For that, the simulation from subsection 7.2 was used. `imgev` is capable of filtering the photons from a given energy interval out of the event file. Thereby three different images were generated: one in the $0.5-2.0\,\mathrm{keV}$ energy band , one in $2.0-5.0\,\mathrm{keV}$ and one in $5.0-8.0\,\mathrm{keV}$. With each of these files an exposure correction as in subsection 7.1 was done. The three images were then combined with `ds9` to a RGB image, where the soft band is red, the medium one is green and the hard one is blue. The final image of that is shown in Figure 7.8.

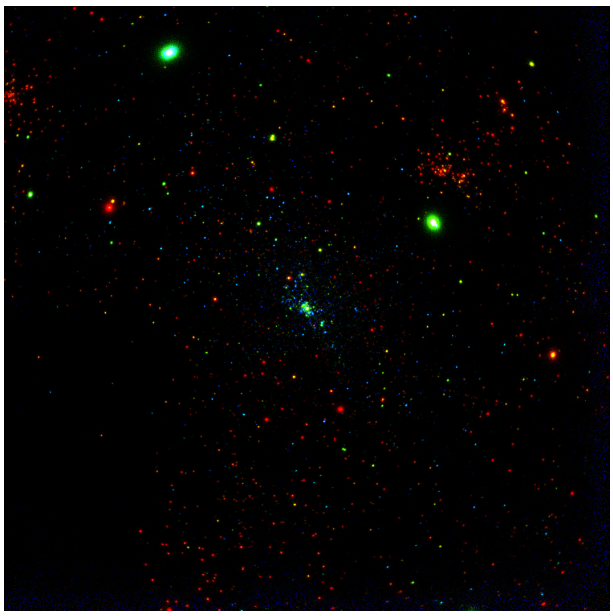

Figure 7.8: RGB image of the three separate simulations of the GC with the WFI and an exposure time of 100 ks each. Red $= 0.5-2.0\,\mathrm{keV}$, Green $= 2.0-5.0\,\mathrm{keV}$, Blue $= 5.0-8.0\,\mathrm{keV}$.

In the image are many red or blue sources visible. The red ones are the sources with a low `kT` ($< 0.2\,\mathrm{keV}$) for their bremsstrahlung spectrum. The blue ones are the hard sources with a power law model and a photon index of 1.51. What that means is that the color of these sources match their N_H value, where the blue ones have a high and the red sources a low N_H. In order to verify this, a map of the N_H of the GC is shown in Figure 7.9 and the field of view of the simulations is indicated with Sgr A* in the center. The bottom left corner of the simulation image is now the bottom corner because of the galactic coordinate system. When comparing now this map to the RGB image, the regions with a low N_H contain the very red sources and in the regions with a higher value the sources are more blue. Apart from that, there are several greenish sources as well. These prove to be the sources with a bremsstrahlung model and higher `kT` values. So all in all, the colors of the sources match their spectral model and N_H.

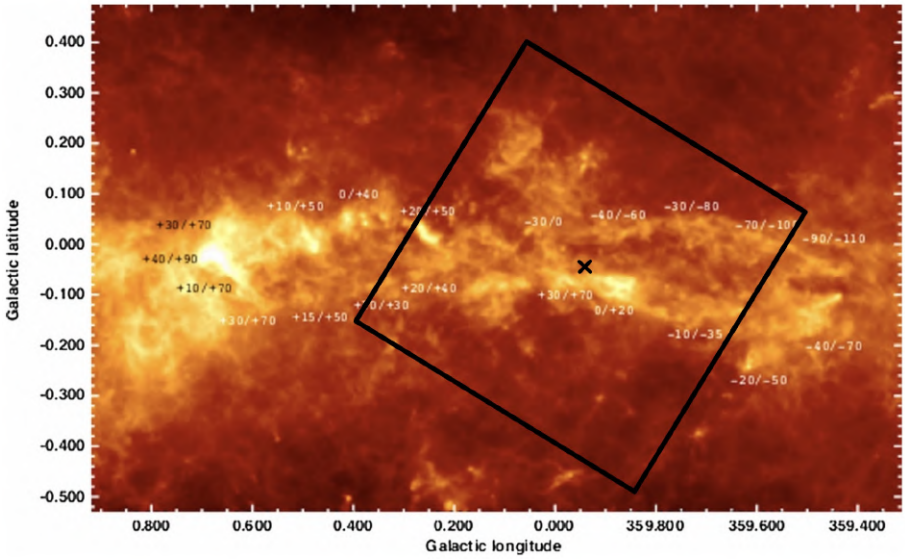

Figure 7.9: Map of the hydrogen column density of the GC with a logarithmic color scale. Minimum: $4 \cdot 10^{22}\,\mathrm{cm}^{-2}$ (dark). Maximum: $4 \cdot 10^{25}\,\mathrm{cm}^{-2}$ (bright). The field of view of the simulations with the WFI is sketched in black. Image from Molinari et al. (2011).

7.5 Source Detection

After the generation of several images, the simulation from subsection 7.2 will be further analyzed. For that, the `wavdetect` tool from CIAO[9] (*Chandra* Interactive Analysis of Observations) was used. It searches for sources in an image and gives a list of these including the right ascension and declination where the tool found them. This is a good measurement in order to test an image of a simulation when comparing the found sources with the ones which were the input of the simulation.
The `sigthresh` value was set to 10^{-6} as it should be about the inverse of the total amount of pixels (image of the simulation with WFI has 1063 x 1063 pixels). Also the exposure map from subsection 7.1 was set as an input file and the `wavelet scales` parameter was set to the suggested $\sqrt{2}$ series (1.0 1.414 2.0 2.828 4.0 5.657 8.0 11.314 16.0). The required point spread function file `psffile` was generated with `dmimgcalc` from CIAO. As a size of the point spread function 5″ was assumed. The input image for the detection run was the simulation from subsection 7.2 without exposure correction.
With these input values `wavdetect` was able to find 2725 sources in the image. This means that about 44 % of the 6201 original sources are detectable. An image of the found sources is shown in Figure 7.10 with a comparison to the image of the simulation.

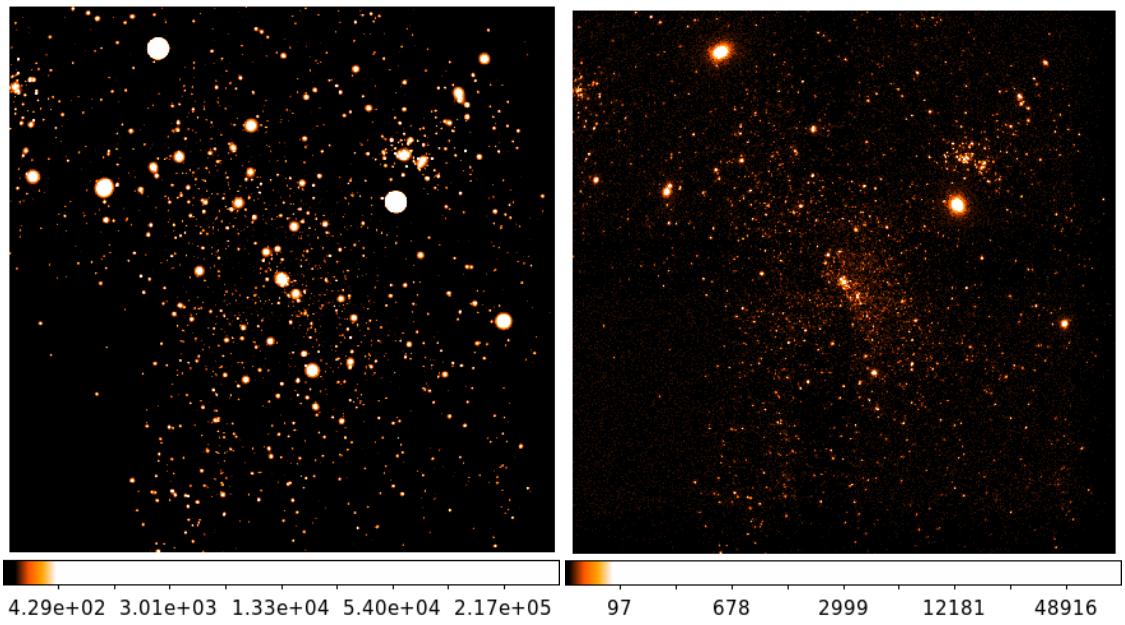

Figure 7.10: Left: Image of the detected sources with `wavdetect` Right: Image of the simulation from subsection 7.2 but without exposure correction. Both scales are in counts.

[9] `https://cxc.cfa.harvard.edu/ciao/`

By comparing the two images, it stands out that the tool finds sources throughout the field of view and that the overall structure of the source distribution is similar. The difference lies in the dense regions, especially in the center around Sgr A*. Here, the tool just shows one bright source because the point sources from the simulation are close together and aren't detectable as individuals. To cover this assumption the detection probability dependent on the distance to the nearest source. For that, the `angular_separation` tool from the `ISISscripts`[10] was used. It calculates the angular distance in degrees between two input sources (right ascension and declination are required). First, this was done for all 6201 sources in the field of view of the simulation. So for every source the nearest distance to another source was calculated and then put into a histogram with a bin width of $1''$ (see Figure 7.11). The same thing was done for the 2725 detected sources in such a way that they were matched to the source in the catalog with the lowest distance and then calculated the nearest separation to the 6201 sources. This also shown in Figure 7.11. Then, the two frequencies of the histograms were divided by each other to get the detection probability as a function of the separation (see Figure 7.11).

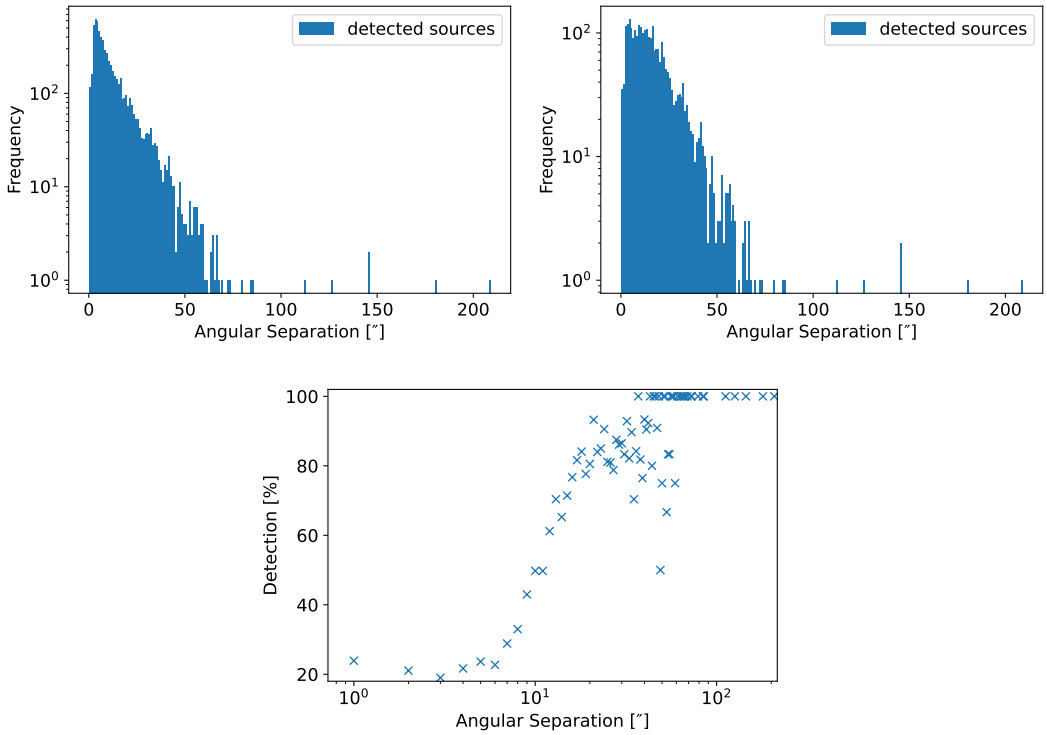

Figure 7.11: Top left: Histogram of all 6201 sources categorized by the nearest distance to the next source. Right: Histogram of the 2725 detected sources dependant on the distance to the closest source of the 6201 sources. Bottom: Detection probability of a source dependent on its separation. All x-axes are in arc seconds.

[10] `https://www.sternwarte.uni-erlangen.de/isis/`

These plots verify the assumption that the amount of detected sources varies with their separation. Almost half of all the sources (2885) have another source in a distance of $6''$ or less. This is also the interval in which the detection probability is the lowest with about 20 %. After that, the amount of detected sources increases progressively with the separation until ca. $18''$. Then the detection is almost always around 80 % or even higher. In the range over $18''$ lie 1155 sources, so around 19 % of all. The few sources with a separation of $60''/1.0'$ or higher have a detection probability of 100 % but it has to be noted that the sample size (24) is very small there.

7.6 *Chandra* Comparison

After all the simulations and analysis of the images for *Athena*, they will now be compared to archived *Chandra* images of the GC. This data can be downloaded as FITS files from the *Chandra* website[11]. There are three images in different energy bands (0.2 – 3.3 keV, 3.3 – 4.7 keV and 4.7 – 8.0 keV) of Sgr A* available. These images come from 43 observations with a total exposure time of about 1 Ms and have a width of 15′.
The simulation was done with the `runsixt` tool because now only one of the four DEPFETs is sufficient to match the field of view. The pointing is now directly on Sgr A* (as there are now no more gaps) and the exposure time was set 50 ks. This value was chosen in order to match the total registered photons in the field of view to the *Chandra* data. *Chandra* has an about 15 times smaller effective area than *Athena* (*Chandra* has $\sim 600\,\mathrm{cm}^2$ at 1.5 keV (Broos et al.; 2010) and *Athena* has $\sim 10000\,\mathrm{cm}^2$ at 1.5 keV (Barret et al.; 2020)) and therefore needs a higher exposure time by that factor. In order to compare the *Chandra* data to the *Athena* simulations, three separate images were generated with the same filtering system for the energy from `imgev` as in subsection 7.4 (now with adjusted bands). The frames were matched to ensure that they show the same region. The final images of the separate energy bands as well as a combined RGB-image are shown in Figure 7.12.
It is noticeable that the overall structure and distribution of the images from the simulation are similar to the *Chandra* images in all energy bands with the central object Sgr A* as the brightest source. However, there are also some prominent differences. The signal-to-noise ratio seems higher in the simulations and there are also more sources as individual points recognizable. The bright sources are more spread and look more extended than in the *Chandra* data. One aspect that contributes to the difference in the images is that the diffuse emission of the GC wasn't incorporated in the simulations. The overall color scheme of the RGB images are also pretty similar. They are both more on the blue side which is caused by the high hydrogen column density in this region with just a few softer sources in the surroundings of Sgr A*. Also, the *Chandra* images look very similar to Figure 3.7 in subsection 3.3. Summarized, *Athena* is capable to produce similar results of the GC with an even higher signal-to-noise ratio (although it has to be noticed that the diffuse emission is missing in the simulations) with an exposure time of just 50 ks compared to the 1 Ms of *Chandra*.

[11] `https://chandra.harvard.edu/photo/openFITS/xray_data.html`

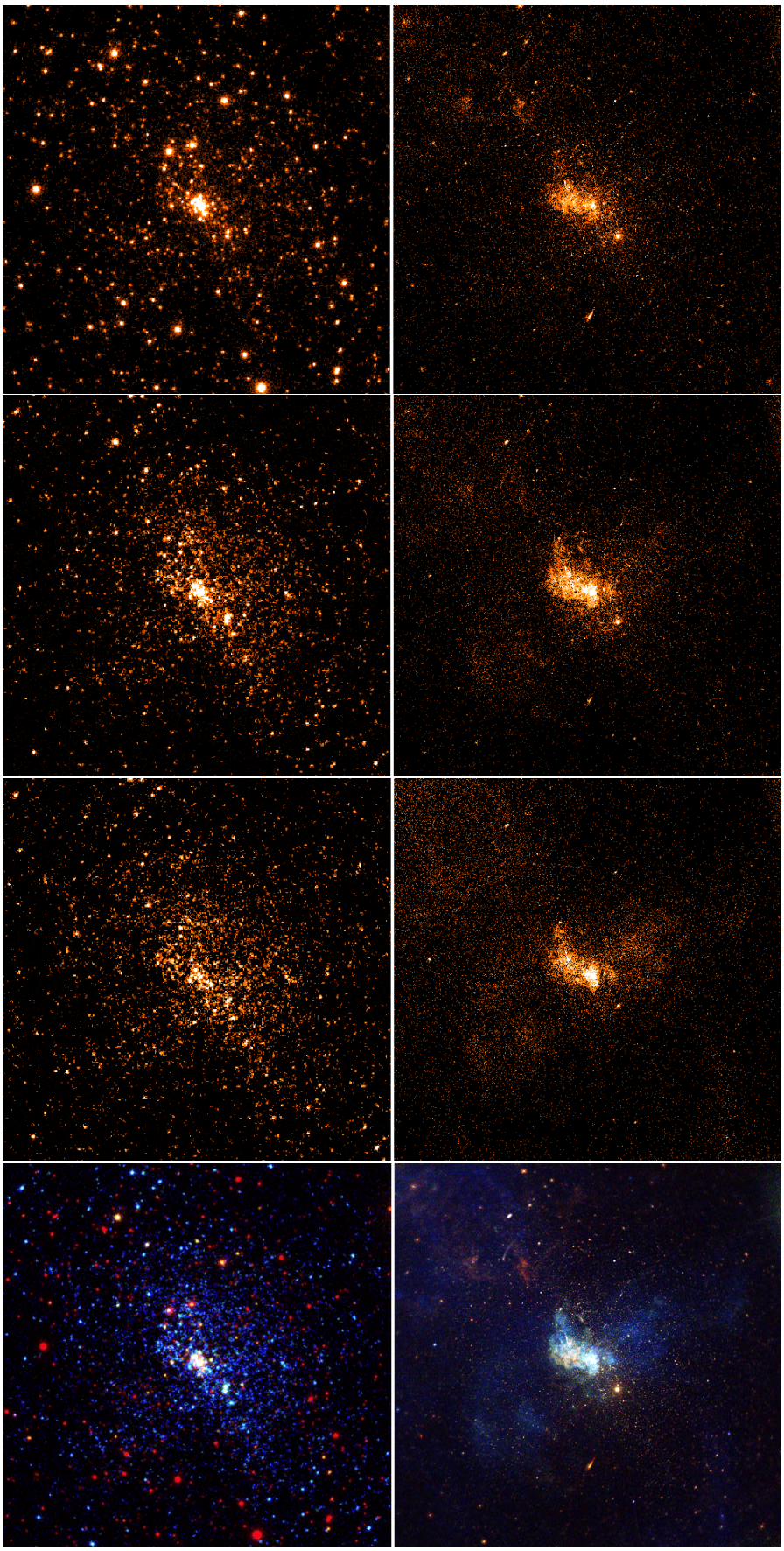

Figure 7.12: Images of the *Athena* simulations (left) and the *Chandra* data (right). First Row = 0.2 – 3.3 keV, Second Row = 3.3 – 4.7 keV, Third Row = 4.7 – 8.0 keV, Fourth Row = RGB-image (red as soft band, green as medium and blue as hard).

8 Summary and Conclusions

In summary, in this thesis I was able to generate an input file for the simulations of the GC by using the *Chandra* catalog from Muno et al. (2009). With that, the final images show pretty impressively the imaging capabilities of the WFI from *Athena*. All of that was possible with an exposure time of just 100 ks, thanks to the large effective area of its optics. By assigning individual spectra to the sources based on their Hardness Ratio, it was possible to receive realistic images of Sgr A and its surroundings. The X-IFU simulation in subsection 7.3 looks as expected less impressive because it is mainly suited for spectroscopy but nevertheless the overall structure of the GC is still visible. In subsection 7.4 I showed an RGB-image where the colors of the sources match their N_{H}. By comparing this image to a map of the hydrogen column density of the GC (Figure 7.9) I found out that the simulations are consistent with that. The red (soft) sources lie in regions with low values while the blue (hard) ones are located in areas with a high N_{H}. After that, I used the CIAO tools in order to identify the sources in the simulation. `wavdetect` found about 44 % of the sources which lie in the field of view of the WFI. I plotted the detection probability as a function of the angular separation of the sources (Figure 7.11) and proved that there is a correlation between them. Sources which have another source in a distance of $6''$ or lower have a detection probability of about 20 %. After that, it increases progressively with the angular separation up to around 80 % and sometimes even 100 %. Finally, in subsection 7.6, I presented a comparison to *Chandra* in different energy bands, as well as a RGB-image and found out that they have an overall very similar structure in all images and colors in the RGB-image while *Athena* just needed 50 ks of exposure time for these results (compared to the 1 Ms of *Chandra*) which is caused by its large effective area.
However, there is still some room for improvement in some aspects of the simulation. First, the variability of the sources and the diffuse emission couldn't be taken into account in this thesis. Muno et al. (2009) found out that about 10 % (856) of the 9017 sources in the catalog show long-term variations (timescale: days to months). 294 sources or 3 % have short term-variability (only a total of 198 after second testing) with timescales of over 10 min. All in all, a total of about 10 % of the sources in the field of view of the simulations with the WFI show any kind of variability. By considering the diffuse emission and the variability, the simulations would be even more realistic and maybe more similar to the *Chandra* images. Another point that could enhance the quality of the final images are the spectra of the sources. In subsection 7.2, I described the process of generating individual spectra based on the HRs of the sources. One problem was that 5825 sources were exclusively detected in the 2.0 – 8.0 keV band and 1127 only in the 0.5 – 2.0 keV band. For the former, a power law with the photon index of 1.51 while for the latter, a thermal bremsstrahlung with a `kT` of 0.187 keV was used. These values are the medians from other sources and therefore the spectra for these are just approximations. By finding separate spectra for each one of these sources, one might also be able to improve the simulations even further.

References

Ayre, M., Bavdaz, M., Ferreira, I., Wille, E., Fransen, S., Stefanescu, A. and Linder, M. (2016). Athena: system studies and optics accommodation, *Space Telescopes and Instrumentation 2016: Ultraviolet to Gamma Ray*, Vol. 9905, SPIE, pp. 623–637.

Baganoff, F. K., Maeda, Y., Morris, M., Bautz, M., Brandt, W., Cui, W., Doty, J., Feigelson, E., Garmire, G., Pravdo, S. et al. (2003). Chandra x-ray spectroscopic imaging of sagittarius a* and the central parsec of the galaxy, *The Astrophysical Journal* **591**(2): 891.

Barret, D., Decourchelle, A., Fabian, A., Guainazzi, M., Nandra, K., Smith, R. and den Herder, J.-W. (2020). The athena space x-ray observatory and the astrophysics of hot plasma, *Astronomische Nachrichten* **341**(2): 224–235.

Barret, D., Trong, T. L., Den Herder, J.-W., Piro, L., Barcons, X., Huovelin, J., Kelley, R., Mas-Hesse, J. M., Mitsuda, K., Paltani, S. et al. (2016). The athena x-ray integral field unit (x-ifu), *Space Telescopes and Instrumentation 2016: Ultraviolet to Gamma Ray*, Vol. 9905, SPIE, pp. 714–754.

Brand, T. (2017). *Detector simulations for the Athena X-ray observatory*, PhD thesis, Friedrich-Alexander-Universität Erlangen-Nürnberg (FAU).

Broos, P. S., Townsley, L. K., Feigelson, E. D., Getman, K. V., Bauer, F. E. and Garmire, G. P. (2010). Innovations in the analysis of chandra-acis observations, *The Astrophysical Journal* **714**(2): 1582.

Bryant, A. and Krabbe, A. (2021). The episodic and multiscale galactic centre, *New Astronomy Reviews* **93**: 101630.

Collon, M. J., Vacanti, G., Günther, R., Yanson, A., Barriere, N., Landgraf, B., Vervest, M., Chatbi, A., van der Hoeven, R., Beijersbergen, M. W. et al. (2016). Silicon pore optics for the athena telescope, *Space Telescopes and Instrumentation 2016: Ultraviolet to Gamma Ray*, Vol. 9905, SPIE, pp. 647–654.

Dauser, T., Falkner, S., Lorenz, M., Kirsch, C., Peille, P., Cucchetti, E., Schmid, C., Brand, T., Oertel, M., Smith, R. et al. (2019). Sixte: a generic x-ray instrument simulation toolkit, *Astronomy & Astrophysics* **630**: A66.

Do, T., Lu, J. R., Ghez, A. M., Morris, M. R., Yelda, S., Martinez, G. D., Wright, S. A. and Matthews, K. (2013). Stellar populations in the central 0.5 pc of the galaxy. i. a new method for constructing luminosity functions and surface-density profiles, *The Astrophysical Journal* **764**(2): 154.

Feldmeier, A., Puls, J. and Pauldrach, A. (1997). A possible origin for x-rays from o stars., *Astronomy and Astrophysics* **322**: 878–895.

Feldmeier-Krause, A., Kerzendorf, W., Neumayer, N., Schödel, R., Nogueras-Lara, F., Do, T., De Zeeuw, P. and Kuntschner, H. (2017). Kmos view of the galactic centre–ii. metallicity distribution of late-type stars, *Monthly Notices of the Royal Astronomical Society* **464**(1): 194–209.

Genzel, R., Eisenhauer, F. and Gillessen, S. (2010). The galactic center massive black hole and nuclear star cluster, *Reviews of Modern Physics* **82**(4): 3121.

Ghez, A., Duchêne, G., Matthews, K., Hornstein, S., Tanner, A., Larkin, J., Morris, M., Becklin, E., Salim, S., Kremenek, T. et al. (2003). The first measurement of spectral lines in a short-period star bound to the galaxy's central black hole: a paradox of youth, *The Astrophysical Journal* **586**(2): L127.

Grimm, H.-J., Gilfanov, M. and Sunyaev, R. (2003). X-ray binaries in the milky way and other galaxies, *Chinese Journal of Astronomy and Astrophysics* **3**(S1): 257.

Güdel, M. (2004). X-ray astronomy of stellar coronae, *The Astronomy and Astrophysics Review* **12**(2): 71–237.

Güdel, M. and Nazé, Y. (2009). X-ray spectroscopy of stars, *The Astronomy and Astrophysics Review* **17**(3): 309–408.

Hensley, K. (2022). First image of the milky way's supermassive black hole, *AAS Nova Highlights* p. 9419.

Heywood, I., Rammala, I., Camilo, F., Cotton, W., Yusef-Zadeh, F., Abbott, T., Adam, R., Adams, G., Aldera, M., Asad, K. et al. (2022). The 1.28 ghz meerkat galactic center mosaic, *The Astrophysical Journal* **925**(2): 165.

Hong, J., Mori, K., Hailey, C. J., Nynka, M., Zhang, S., Gotthelf, E., Fornasini, F. M., Krivonos, R., Bauer, F., Perez, K. et al. (2016). Nustar hard x-ray survey of the galactic center region. ii. x-ray point sources, *The Astrophysical Journal* **825**(2): 132.

Hong, J., Van den Berg, M., Grindlay, J. E. and Laycock, S. (2009). Radial distribution of x-ray point sources near the galactic center, *The Astrophysical Journal* **706**(1): 223.

Kenyon, S. J., Brown, D. I., Tout, C. A. and Berlind, P. (1998). Optical spectroscopy of embedded young stars in the taurus-auriga molecular cloud, *The Astronomical Journal* **115**(6): 2491.

Lucy, L. B. and White, R. (1980). X-ray emission from the winds of hot stars, *The Astrophysical Journal* **241**: 300–305.

Mauskopf, P. (2018). Transition edge sensors and kinetic inductance detectors in astronomical instruments, *Publications of the Astronomical Society of the Pacific* **130**(990): 082001.

Meidinger, N., Nandra, K., Rau, A., Plattner, M. and WFI proto-Consortium (2015). Wide Field Imager for Athena, *Exploring the Hot and Energetic Universe: The first scientific conference dedicated to the Athena X-ray observatory*, p. 5.

Molinari, S., Bally, J., Noriega-Crespo, A., Compiegne, M., Bernard, J., Paradis, D., Martin, P., Testi, L., Barlow, M., Moore, T. et al. (2011). A 100 pc elliptical and twisted ring of cold and dense molecular clouds revealed by herschel around the galactic center, *The Astrophysical journal letters* **735**(2): L33.

Mossoux, E., Finociety, B., Beckers, J.-M. and Vincent, F. (2020). Continuation of the x-ray monitoring of sgr a*: the increase in bright flaring rate confirmed, *Astronomy & Astrophysics* **636**: A25.

Muno, M. P., Bauer, F. E., Baganoff, F. K., Bandyopadhyay, R. M., Bower, G. C., Brandt, W. N., Broos, P. S., Cotera, A., Eikenberry, S. S., Garmire, G. P., Hyman, S. D., Kassim, N. E., Lang, C. C., Lazio, T. J. W., Law, C., Mauerhan, J. C., Morris, M. R., Nagata, T.,

Nishiyama, S., Park, S., Ramìrez, S. V., Stolovy, S. R., Wijnands, R., Wang, Q. D., Wang, Z. and Yusef-Zadeh, F. (2009). A Catalog of X-Ray Point Sources from Two Megaseconds of Chandra Observations of the Galactic Center, **181**(1): 110–128.

Pike, S. N., Harrison, F. A., Tomsick, J. A., Bachetti, M., Buisson, D. J., García, J. A., Jiang, J., Ludlam, R. M. and Madsen, K. K. (2021). Photospheric radius expansion and a double-peaked type-i x-ray burst from grs 1741.9–2853, *The Astrophysical Journal* **918**(1): 9.

Raman, G., Paul, B., Bahal, V. and Iyer, N. (2018). Detection of type-1 bursts from the Galactic Center using Astrosat-LAXPC, *42nd COSPAR Scientific Assembly*, Vol. 42, pp. E1.6–36–18.

Reig, P. (2011). Be/x-ray binaries, *Astrophysics and Space Science* **332**(1): 1–29.

Stolte, A. (2013). Massive Star Clusters and the high-mass population in the Galactic center, *Massive Stars: From alpha to Omega*, p. 30.

Tauris, T. and Van Den Heuvel, E. (2006). Formation and evolution of compact stellar x-ray sources, *Cambridge Astrophysics Series* **39**: 623.

Witzel, G., Sitarski, B., Ghez, A. M., Morris, M. R., Hees, A., Do, T., Lu, J. R., Naoz, S., Boehle, A., Martinez, G. et al. (2017). The post-periapsis evolution of galactic center source g1: the second case of a resolved tidal interaction with a supermassive black hole, *The Astrophysical Journal* **847**(1): 80.

Zhao, J.-H., Blundell, R., Moran, J. M., Downes, D., Schuster, K. F. and Marrone, D. P. (2010). The high-density ionized gas in the central parsec of the galaxy, *The Astrophysical Journal* **723**(2): 1097.

Zwart, S. F. P., Makino, J., McMillan, S. L. and Hut, P. (2002). The lives and deaths of star clusters near the galactic center, *The Astrophysical Journal* **565**(1): 265.

Acknowledgements

I would like to thank my research supervisor Jörn Wilms for this opportunity to work at the observatory and write my thesis about this topic. I was able to expand my knowledge and immerse myself in a fascinating field of astronomy.
I also want to express my thanks to the whole SIXTE team (Thomas Dauser, Maximilian Lorenz, Lea Michalski, Christian Kirsch and Ole König) for the help and answers to my questions about the simulations and images.
I am grateful to everyone at the Remeis observatory I had the pleasure to meet and talk with.

Eidesstattliche Erklärung

Ich erkläre hiermit, dass ich die vorliegende Arbeit selbständig verfasst, andere als die angegebenen Quellen/Hilfsmittel nicht benutzt, und die den benutzten Quellen wörtlich und inhaltlich entnommenen Stellen als solche kenntlich gemacht habe.

Oberasbach, am 23.08.2022 .....

Matthias Rohe